Experiments in Fluids (2024) 65:156
https://doi.org/10.1007/s00348-024-03881-2

RESEARCH ARTICLE

Skin-friction from temperature and velocity data around a wall-mounted cube

Massimo Miozzi[1] · Andreas Schröder[2,4] · Daniel Schanz[2] · Christian E. Willert[3] · Christian Klein[2] · Jonathan Lemarechal[2]

Received: 17 May 2024 / Revised: 2 September 2024 / Accepted: 5 September 2024

Abstract

This paper reports an algorithm for measuring the time-averaged skin friction vector field $\overline{\boldsymbol{\tau}}(\boldsymbol{X})$ starting from time-resolved temperature maps, acquired by a functional coating of temperature-sensitive paint. The algorithm is applied to a large area around a wall-mounted cube, immersed in the turbulent boundary layer over a flat plate. The method adopts a relaxed version of the Taylor Hypothesis operating on time-resolved maps of temperature fluctuations T' measured on the slightly warmer bounding surface. The procedure extracts $\overline{U}_T(\boldsymbol{X})$, the celerity of displacement of T', as the best approximation of the forecasting provided by the frozen turbulence assumption near the wall, where its rigorous application is inappropriate. The $\overline{\boldsymbol{\tau}}(\boldsymbol{X})$ estimation is based on the hypothesis of a linear relationship between $\overline{U}_T(\boldsymbol{X})$ and $\overline{U}_U(\boldsymbol{X})$, chained to the one between $\overline{U}_U(\boldsymbol{X})$ and $\overline{U}_\tau(\boldsymbol{X})$. We assess the outcomes of the proposed algorithm against those derived by the 2D and 3D Lagrangian particle tracking (LPT) methodology 'Shake-The-Box', whose advent has made available high-quality near-wall flow field information. Furthermore, data from high-density 2D time-resolved LPT allows exploring the suitability of the linear relationships chain between $\overline{U}_T(\boldsymbol{X})$ and $\overline{U}_\tau(\boldsymbol{X})$ in the proposed context.

1 Introduction

Widely speaking, a fluid flowing around a bluff body complies with a *no-slip* condition at the wall. Accordingly, it exerts a shear force on the body's surface, the skin friction vector field $\boldsymbol{\tau}(\boldsymbol{X}_\pi, t) = \mu \partial \boldsymbol{U}(\boldsymbol{X}, t)/\partial Y|_{wall}$, defined on the plane $\boldsymbol{X}_\pi$ locally tangent to the surface spanned by axes X and Z at point $P \equiv [X, 0, Z]$. Its magnitude relies on the slope of the wall-parallel velocity components' vertical profile in P. At the same time, close to the wall, passive scalars like velocity and temperature fluctuations displace at a celerity of propagation larger than the vanishing speed of the surrounding flow (Eckelmann 1974). Based on the relationship between such celerities and the friction velocity $\boldsymbol{U}_\tau(\boldsymbol{X}_\pi, t) = \sqrt{\boldsymbol{\tau}(\boldsymbol{X}_\pi, t)/\rho}$ (Eckelmann 1974; Kim and Hussain 1993; Hetsroni et al. 2004; Del Álamo and Jiménez 2009), this paper presents an algorithm to estimate the time-averaged $\overline{\boldsymbol{\tau}}_T(\boldsymbol{X}_\pi)$ from time histories of temperature fluctuations and describes its application to the 3D flow around a wall-mounted cube. The algorithm enhances the method based on a relaxed form of the Taylor Hypothesis proposed in Miozzi et al. (2020) (named TH algorithm in the following). To attempt an assessment of the method, the friction velocity $\overline{\boldsymbol{U}}_{\tau_T}$ and the skin friction $\overline{\boldsymbol{\tau}}_T$ are compared against

Massimo Miozzi, Andreas Schröder, Daniel Schanz, Christian E. Willert, Christian Klein and Jonathan Lemarechal have contributed equally to this work.

✉ Massimo Miozzi
massimo.miozzi@cnr.it

Andreas Schröder
andreas.schroeder@dlr.de

Daniel Schanz
daniel.schanz@dlr.de

Christian E. Willert
chris.willert@dlr.de

Christian Klein
christian.klein@dlr.de

Jonathan Lemarechal
jonathan.lemarechal@dlr.de

[1] CNR-INM, National Research Council, Institute of Marine Engineering, 00128 Rome, Italy

[2] DLR, German Aerospace Center, 30373 Göttingen, Germany

[3] DLR, German Aerospace Center, 51147 Köln, Germany

[4] BTU Cottbus-Senftenberg, 03046 Cottbus, Germany

Published online: 15 October 2024

the similar quantities $\overline{\boldsymbol{U}}_{\tau_V}$ and $\overline{\boldsymbol{U}}_{\tau_V}$ derived from 2D and 3D STB particle tracking-based experimental results carried out in the same facility and described in Schröder et al. (2020). The subscripts $(.)_T$ and $(.)_V$ indicate the data from which the subscribed quantity originates (the temperature at the wall or the flow velocity, respectively).

The comparison concerns the topology and the magnitude of the skin friction vector fields. Comparing two vector fields on a topological basis implies comparing their topological equivalence, focusing on the correspondence between their critical points: saddles with saddles, sources with sources, sinks with sinks, etc. After checking the critical points correspondence, the comparison moves to their location. The topological check supplies a solid framework to survey the local matching level between the vector's intensities.

Notwithstanding its apparent simplicity, the presence of a wall-mounted cube causes, in the flow around the protrusion, the genesis of a variety of complex coherent structures around each side of the obstacle, and its study has been the subject of investigation for a long time now. A brief portrait of them (see Fig. 1) shows the incoming flow generating separation in front of the cube and on its lateral sides. Downstream of the cube, a reverse flow region behaves with the typical quasi-periodic behavior of a bluff-body wake. Within this region, recirculation forces the flow to arrange in an arc-shaped vortex before recovering the incoming stream. Each of these structures contributes peculiarly and differently to the composition of the skin friction vector field. The remarkable complexity of the flow is shown in Fig. 1, which suggests this setup to be an ideal candidate for evaluating the capabilities and limits of the TH algorithm.

First studies on this kind of flow focused on the onset of the large horseshoe-shaped vortex structures developing around the obstacle (Baker 1980). It was Martinuzzi and Tropea (1993) that reported the first and complete quantitative descriptions of the 3D flow around a wall-mounted cube, representing the whole flow-obstacle interaction as a system of large-scale, horseshoe-shaped vortices generated upstream, which develops horizontally around the cube surrounding smaller-scale coherent structures set on the cube faces (see Fig. 1). Among these, the arc-shaped vortex plays a major role in the adverse pressure gradient region immediately downstream of the obstacle.

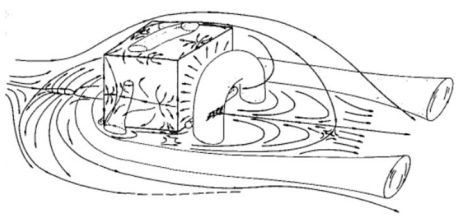

Fig. 1 A sketch of the mean 3D flow around a surface-mounted cube (Martinuzzi and Tropea 1993)

Subsequent papers on the subject have contributed to the discussion up to the present day, both from experimental and numerical points of view, see e.g. Schröder et al. (2020), Gao et al. (2021), Yakhot et al. (2006), Diaz-Daniel et al. (2017) and da Silva et al. (2021), among the others.

Contrasting to the attention devoted to the large structures surrounding the obstacle, relatively little interest concerned the near-wall flow, especially from the experimental point of view, most likely due to the challenging obstacles imposed by the measurement. Limitations of oil-film-based techniques (Tian et al. 2004; Depardon et al. 2005) suggested that the estimation of $\overline{\boldsymbol{\tau}}$ could be more reliably obtained by near-wall PIV measurements rather than the oil-film approach. In particular, Depardon et al. (2005) adopted the critical point analysis to characterize and investigate friction velocity fields obtained by oil film technique and near-wall 2D PIV measurement on the set of planes extending from 0.5 to 5 mm distance to the wall. More recently, Gao et al. (2021) reported on 3D measurements around two small cubes of 1mm in size (equivalent to $91Y^+$) placed side-by-side in a turbulent channel flow. Using microscopic dual-view tomographic holography the achievable resolution for the average 3D flow field is high enough to allow estimation of the wall shear field.

The present paper is organized as follows: Sect. 2 describes the TSP and STB measurement techniques. Section 3 reports on the skin friction estimation approaches adopted in this paper, while their application to the experiments is described in Sect. 4. Section 5 describes the crucial phases of the data preprocessing, while results are reported in Sect. 6. Summarizing comments and conclusions are provided in Sect. 7.

2 The skin friction measurement techniques

2.1 Available measurement methods

A wide variety of different procedures are available for the measurement of the skin friction vector field $\boldsymbol{\tau}$ or its streamwise component (see e.g. Tropea et al. 2007 and Sections 12.2.1-2 within). The approaches can be classified as *indirect* and *direct*. The former ground on the derivation of the skin friction from the measure of some other quantity like velocity, heat transfer or pressure, while the latter attempts to measure the friction force directly by floating elements flush mounted on the body surface, or with oil films placed on the wall. Recent technological developments have made available methods for the estimation of instantaneous, spatially resolved $\boldsymbol{\tau}(t, x)$ (see e.g. Örlü and Vinuesa 2020

and references within), whose level of accuracy still requires further improvements.

2.2 Temperature-sensitive paint

The temperature-sensitive paint method (see Liu et al. 2021 for extensive review and references) is an optical measurement technique to measure surface temperatures. Its classical implementation consists of a transparent paint doped with temperature-sensitive dye molecules. When these molecules are excited by light with an appropriate wavelength, their electrons move to an excited state and rapidly decay in a time scale ranging between $O(10\,\text{ns})$ and $O(1\,\text{ms})$. The return to the ground state occurs predominantly by a radiationless process (thermal quenching) or by emitting light with a larger wavelength (Stokes shift). The emitted light intensity is inversely proportional to the local temperature and can be acquired by a standard digital imaging device. The surface temperature distribution can be determined after a proper calibration for a known set of temperatures (Liu et al. 1995; Cattafesta et al. 1998). In aerodynamic and hydrodynamic applications, TSP is used for heat-flux measurements (Liu et al. 1995; Nakakita et al. 2003; Ozawa et al. 2014; Risius et al. 2017), time-resolved surface-based flow visualizations (Fey and Egami 2007; Capone et al. 2015; Lemarechal et al. 2019; Miozzi et al. 2019), transition localization (Asai et al. 1996; Fey and Egami 2007; Miozzi et al. 2019), and skin friction measurements based on different methods: Colburn Analogy (Lemarechal et al. 2021) and the relaxed version of the Taylor Hypothesis here proposed (Miozzi et al. 2020). These TSP applications require an artificial heat flux between the model surface and the surrounding fluid to sufficiently enhance the temperature differences (Fey and Egami 2007). Besides changing the fluid temperature (Gartenberg et al. 1990), heating the surface with an infrared laser (Klein et al. 2020), warmer water flowing through the model (Capone et al. 2015; Miozzi et al. 2019), an integrated model heating based on carbon nanotubes (Klein et al. 2014) or current-carrying carbon fibers in an epoxy matrix (Lemarechal et al. 2019; Klein et al. 2023) are established methods to generate the heat flux.

It is noteworthy that the quenching effect induced by the thermal inertia of the TSP coating, considered as a "thin" layer, introduces an upper limit on the frequency and wavenumber of the thermal structures measurable with the TSP at the body surface (Astarita and Carlomagno 2012; Nakamura 2009). In other words, the measurement can not completely capture the actual temperature of the viscous sublayer in both time and space. The upper limit on frequency and wavenumber induced by thermal quenching acts as a selective filter. The upper limit on wavenumbers cuts out the signature of smaller T' disturbances. In contrast, the upper limit on frequencies will dampen faster flow structures with shorter residence times. This would introduce a bias in the measurement of the temperature fluctuations T', which can be quantified by checking the frequency/wavenumber response of the paint against the physical characteristics of the flow.

2.3 Shake-the-box

Shake-The-Box (STB) is a method to volumetrically track a large number of tracer particles in a flow, using time-resolved projections of the particles onto several cameras (Schanz et al. 2016). Suitable seeding particles are evenly distributed in the flow and a measurement volume is illuminated using either an expanded laser beam or arrays of high-power LEDs. The illumination is pulsed and synchronized to the framing rate of a multi-camera system, which views the measurement volume from different directions, thereby freezing the particle movement within each image. The 3D position of the particles can be reconstructed from the different projections using recently introduced triangulation techniques; STB uses the advanced Iterative Particle Reconstruction (IPR) technique (Wieneke 2012; Jahn et al. 2021). For accurate results, the camera system has to be thoroughly calibrated using a suitable calibration target, the application of Volume-Self-Calibration (Wieneke 2008) and the calibration of the optical transfer function of the particle images (Schanz et al. 2013). Despite the efforts on calibration and the use of the most advanced reconstruction algorithms, single time-steps would—under experimental conditions—still be limited to relatively low particle image densities to allow for a good reconstruction quality. STB significantly shifts this limit by making use of a predictor/corrector step, which elongates tracked particles and corrects for any prediction errors by 'shaking' the predicted particles to their correct locations using a gradient descent scheme, operating on the local residual image. This step allows correct positioning of all tracked particles prior to any reconstruction efforts and leads to a convergence of the algorithm to a state, where only particles newly entering the measurement domain have to be identified using advanced IPR. The usable seeding densities can exceed 0.1 particles-per-pixel (ppp) under very good viewing conditions, allowing to track hundreds of thousands of particles instantaneously. For the experiment discussed here, the seeding densities attained for the 3D STB are lower due to a distinct polydispersity of the seeding material. In contrast, excellent seeding densities are achieved for measurement by 2D STB. This technique was applied limited to three planar patches along the symmetry plane, having dimensions $8\ \text{mm} \times 15\ \text{mm}$ (see Sect. 4). For a more comprehensive overview of Lagrangian Particle

Tracking techniques, the reader is referred to Schröder and Schanz (2023).

3 Skin-friction estimation

3.1 Skin-friction from temperature data

3.1.1 The structure of the viscous sublayer

Eckelmann (1974) first noticed the *surface flow* of velocity fluctuations in a Turbulent Boundary Layer (TBL) over a flat plate. Using an *ad hoc* designed oil-channel facility, he carefully estimated the fluctuating wall-normal gradient of the streamwise velocity at the wall $\partial U(Y,t)/\partial Y\big|_{wall}$ and the fluctuating velocity $u(Y, t)$ at different wall distances Y. For increasing wall distanced $Y^+ = YU_\tau/\nu$ he observed an identical evolution in time up to $Y^+ < 10$ along with an increasing phase decoupling at farther wall distances (see Eckelmann 1974 and Fig. 6 within). Despite the expected no-slip condition at the wall and the associated monotonic vanishing of U for $Y \to 0$, the velocity fluctuations behave like a wave, propagating faster than the surrounding flow. For that reason, we adopt the term *celerity* to indicate the propagation speed U_q of the fluctuations q of a generic passive scalar $Q = \overline{Q} + q$.

Kim and Hussain (1993) used a Direct Numerical Simulation (DNS) of a turbulent channel flow to investigate the propagation celerity of the fluctuating velocity and vorticity components. The peak position of the two-point space-time correlation function estimates the space lag ΔX_{max} corresponding to a fixed time lag Δt. Below $Y^+ < 10$ the celerity of propagation of velocity disturbances is in a constant ratio with the friction velocity. This linear relationship is expressed in Kim and Hussain (1993) as:

$$\boldsymbol{U}_u = c_u \cdot \boldsymbol{U}_\tau \tag{1}$$

where $c_u = 9 - 10$ (Kim and Hussain 1993; Geng et al. 2015). Whether the parameter c_u can be represented only by a scalar or should be considered a more complex dependence, and whether it is influenced by the local pressure gradient rather than the Reynolds number, are still open questions (Liu et al. 2024) that we would like to help clarify within the limits of this work.

Kim and Hussain (1993) also found a dependency of the streamwise-oriented U_u on Δt, which is negligible away from the wall but becomes important close to the wall ($Y^+ < 10$). In that region, U_u exhibits a scale dependency induced by coherent structures at different wave-number, that undergo the influence of more or less intense external flow $U(Y)$. Smaller structures are associated with slower motion, while larger ones displace faster. Having in mind that a complete description of the displacement of coherent structures requires the characterization of their *dispersion relationship* in the wave-number–frequency plane $k - \omega$, Del Álamo and Jiménez (2009) proposed a physically-motivated relation to extract U_u based on the minimization of the discrepancies between the measured results and what supposed by the Taylor Hypothesis applied on a channel flow, having U_u as the reference frame velocity. This approach relaxes the Taylor Hypothesis and makes available its use even where the unreliability of the Taylor Hypothesis itself is well known, such as near the wall.

3.1.2 Relaxation of the Taylor hypothesis

The Taylor Hypothesis, as defined in Taylor (1938), assumes that the gradients of U do not evolve significantly as coherent structures advect past the sensor, as long as "the velocity of the airstream which carries the eddies is very much greater than the turbulent velocity". The passage of a *frozen* pattern of a passive scalar over the measurement point can be expressed, for a generic fluctuating quantity q, as:

$$\frac{Dq}{Dt} = \frac{\partial q}{\partial t} + \boldsymbol{U}_q \cdot \nabla q = 0 \tag{2}$$

where $\boldsymbol{U}_q$ is the framework velocity of the turbulent pattern, typically assimilated to the local mean velocity. Among the approvals and criticisms about the effectiveness of Taylor's Hypothesis, there is general agreement that the *frozen turbulence* condition does not hold near the wall because of the strong shear production characterizing that region and because of the failure to comply with the requirement $|u/U| \ll 1$.

The physics-based approach proposed by Del Álamo and Jiménez (2009) relaxes the *frozen* requirement by assuming that the turbulent framework is advected at a celerity that minimizes the discrepancies between the forecast by the Taylor Hypothesis and the measurements. This leads to the following:

$$\begin{aligned} \frac{Dq}{Dt}\bigg|_m in = \varepsilon = \overline{(\partial q/\partial t + \boldsymbol{U}_q \cdot \nabla q)^2}\Big|_{min} \\ \Rightarrow \frac{\partial}{\partial U_i}\left\{\overline{(\partial_t + U_1\partial_1 + U_2\partial_2)^2}\right\} = 0 \end{aligned} \tag{3}$$

where the term $i = 1, 2$ indicates orthogonal directions lying on the plane π tangent to the wall at point P, ∂_t and ∂_i, $i = 1, 2$ are the time and space derivatives, and ε is an arbitrarily small quantity. In the lower expression of Eq. 3 and in the following, the term q is omitted from the celerity components U_i and the differential operators $\partial_{i,t}$ without ambiguity. The expression for the propagation celerity components of $\boldsymbol{U}_q$ from Eq. 3 states (Liu et al. 2024):

$$\begin{cases} U_1 = (-\overline{(\partial_2)^2}\cdot\overline{\partial_1\partial_t} + \overline{\partial_2\partial_t}\cdot\overline{\partial_1\partial_2}) \,/\, (\overline{(\partial_1)^2}\cdot\overline{(\partial_2)^2} - (\overline{\partial_1\partial_2})^2) \\ U_2 = (-\overline{(\partial_1)^2}\cdot\overline{\partial_2\partial_t} + \overline{\partial_1\partial_t}\cdot\overline{\partial_1\partial_2}) \,/\, (\overline{(\partial_1)^2}\cdot\overline{(\partial_2)^2} - (\overline{\partial_1\partial_2})^2) \end{cases} \tag{4}$$

If the correlation between the derivatives of q along orthogonal directions on the plane π is negligible, i.e. the term $\overline{\partial_1\partial_2} \approx 0$, then Eq. 4 reduces to Del Álamo and Jiménez (2009):

$$\begin{cases} U_1 = -(\overline{\partial_1\partial_t}) \,/\, (\overline{(\partial_1)^2}) \\ U_2 = -(\overline{\partial_2\partial_t}) \,/\, (\overline{(\partial_2)^2}) \end{cases} \tag{5}$$

If the previous condition holds and the homogeneous direction 1 is aligned streamwise, $(\overline{\partial_1^2}\cdot\overline{\partial_2^2} - (\overline{\partial_1\partial_2})^2) = 0$ and Eq. 5 reduces to:

$$\begin{aligned} U_1 &= -\frac{\overline{\partial_1\partial_t}}{\overline{(\partial_1)^2}} \\ U_2 &= 0 \end{aligned} \tag{6}$$

3.1.3 From the celerity of temperature to that of velocity fluctuations

The existence of a linear relationship between the celerity of propagation of velocity disturbances U_u and the friction velocity U_τ in Eq. 1 suggests adopting one of Eqs. 4, 5 or 6 to calculate the propagation celerity U_T of temperature fluctuations, then move back to the friction velocity U_τ. By definition, the momentum and thermal diffusivity coincide only if the Prandtl number $Pr = \nu/\alpha$ is unity, implying equal values for the kinematic viscosity ($\nu = \mu/\rho$) and the thermal diffusivity ($\alpha = k/\rho(C_p)$). In water (with $Pr \approx 7.5$ at $T \approx 21°C$) the condition $Pr = 1$ does not hold and thus it is necessary to account for the different diffusivity of momentum and temperature to modulate the coefficient c_u in Eq. 1 with a proper constant c_T.

Hetsroni et al. (2004) provided a criterion that put together the diffusivity of momentum and temperature, starting from the thermal conditions applied to the boundaries. This criterion states that the celerity of propagation of temperature and velocity fluctuations are related by a power expression of the Prandtl number, whose magnitude depends on the boundary conditions (B.C.):

$$U_T^+ = c_T \cdot U_u^+ = c_T \cdot c_U \cdot U_\tau \tag{7}$$

$$c_T = Pr^{-1/3} \quad \text{for isothermal B.C.} \tag{8}$$

$$c_T = Pr^{-1/2} \quad \text{for constant heat flux B.C.} \tag{9}$$

3.1.4 From the celerity of velocity fluctuations to friction velocity

The nature of the coefficients c_u and c_T in Eqs. 1 and 7 has been explored in the past by numerical and experimental investigations, in canonical flow conditions like channel flows or turbulent, zero, or adverse pressure gradients (ZPG, APG) boundary layers. Recently, Dròżdż et al. (2023) reported on an experimental study about the influence of the APG on the convective velocity U_u across the boundary layer thickness in a flat plate. The authors use two-point measurements to estimate U_u via cross-correlation and three Clauser-plot inspired strategies for the U_τ estimation, each valid in a certain interval of Re. Their parametric exploration around the friction Reynolds number $Re_\tau = U_\tau\delta^\star/\nu$, the form factor $H = \delta^\star/\theta$, and the Clauser-Rotta pressure parameter $\beta = \frac{\delta^\star}{\tau}\frac{dPe}{dx}$ illustrates the negligible U_u evolution below $Y^+ = 100$ for $\beta < 19$, and a larger variation for $\beta > 19$. Currently, no attempt has been made to establish the relationship between U_τ and U_u in complex flows, with the simultaneous presence of favorable and adverse pressure gradients, and disclaiming any preliminary hypothesis on the flow (like in the Clauser plot procedure) and on the coefficients (e.g. the implicit hypothesis on their scalar nature).

To shed light on such a challenging relationship, here we report the attempt to extract U_u, characterize its relationship with u_τ, and investigate the scalar/tensorial nature of c_U by relying uniquely on the measured quantities in the fluid and at the wall, avoiding any prejudicial hypothesis and quantification. To this aim, the following reports a specific investigation on c_U based on the velocity field results in the middle plane from the 2D-2C STB data, where $\overline{U}_U$ extracted by Eq. 6 is compared against $\overline{U}_\tau$ estimated by the wall-normal profile using Eq. 12 provided in the following section.

3.2 Skin-friction from LPT velocity data

Near-wall time-averaged or instantaneous velocity fields, obtained from LPT data on wall-normal planes or volumes by bin-averaging or interpolation of particles located within the viscous sublayer ($Y < 5Y^+$), can be used to estimate the skin-friction and the friction velocity components along the streamwise and spanwise directions $i = 1, 2$ lying on the plane π locally tangent to the wall, by following the classical relationships (Schlichting and Gersten 2017):

$$\overline{\boldsymbol{\tau}}_w(\boldsymbol{X}) = \mu \lim_{Y\to 0} \partial\overline{\boldsymbol{U}}_w/\partial Y \approx \mu\, \Delta\overline{\boldsymbol{U}}_w/\Delta Y \tag{10}$$

$$\overline{\boldsymbol{U}}_\tau(\boldsymbol{X}) = \sqrt{\overline{\boldsymbol{\tau}}_w/\rho} \tag{11}$$

$$\overline{\boldsymbol{U}}_{\tau}(\boldsymbol{X}) = \sqrt{\nu \frac{\partial \overline{\boldsymbol{U}}_{w}}{\partial Y}} \approx \sqrt{\nu \frac{\Delta \overline{\boldsymbol{U}}_{w}}{\Delta Y}} \tag{12}$$

where the subscript $(.)_w$ indicates quantities at the wall. The calculus of the wall-normal velocity derivative as close to the surface as possible (in the limit of $Y^+ \rightarrow 0$) requires the knowledge of the flow velocity in a region challenging for particle-based measurement methods. In particular, issues related to light reflection, light plane thickness, and optical access are coupled with the difficulties in providing seeding of mono-dispersed size and gaining uniform particle distribution because of the presence of the wall and recirculating regions. However, since LPT methods do not rely on correlation windows (whose reliability would severely suffer from a locally low particle density and the strong shear close to the wall), the resolution of 3D STB averaged results can be enhanced by simply extending the measuring time, thereby increasing the available particle data. The volumetric results presented here show that relatively few samples (100-500) are sufficient for acceptable time-averaged results, due to the low level of fluctuations within the viscous sublayer. In addition, 2D time-resolved tracking results were obtained with higher particle density, supplementing the 3D results with a significantly large database in a subdomain in front of the cube.

4 The experiments

4.1 Experimental setups

The LPT and TSP experimental campaigns have been conducted at the THBV low-speed water tunnel (ONERA, Lille - FR). It is a gravity-driven, closed-loop water tunnel equipped with excellent optical access, therefore making it ideally suited for particle- and laser-based velocimetry as well as luminescence intensity-based thermometric techniques. The test section is 300 mm × 300 mm in size and can be operated at free-stream velocities ranging from 0.01m/s to 1.5m/s. The boundary layer flow is generated on a splitting plate with an elliptical leading edge, placed in the center plane (see Fig. 2). A cube made of glass, $H = 10$ mm in edge length, is located at 510 mm downstream of the leading edge. A 2D step of 1.5 mm height spanning the splitting plate trips the development of a low Reynolds number turbulent boundary layer. The step is inserted into the groove near the leading edge of the plate shown in Fig. 2. Downstream of the leading edge, different flat plates have been designed to satisfy the requirements of the specific measurement technique as follows.

TSP surface temperature: experimental set-up. The TSP measurements were conducted on a flat plate with the same spatial properties as for the STB measurement and with the same glass cube at the same location. The flat plate for TSP measurements starts directly downstream of the leading edge module as shown in Fig. 2. It is equipped with integrated electrical heating and coated with a polyurethane clear coat, doped with a Europium-based luminophore having high temperature sensitivity (−3.3%/K at 20 °C), high emission and negligible pressure sensitivity (Ondrus et al. 2015). The suitability of this TSP coating for applications in water was previously established (Lemarechal et al. 2021). The integrated electrical heating is based on a current-carrying layer of carbon fiber (Fey and Egami 2007; Lemarechal et al. 2019; Klein et al. 2023) in a layup of fiber-reinforced plastic. This heating layer (295 mm × 580 mm) has a resistance of 0.7 Ω and is electrically insulated by layers of glass fiber-reinforced plastic. For further insulation, a foil of stainless steel is integrated into the fiber-reinforced plastic to counteract a reduction of the electrical insulation by water diffusion into the epoxy. The overall thickness of the fiber-reinforced plastic part is approximately 0.5 mm. This part was manufactured in a negative mold, i.e., the manufacturing was started with the TSP coating, as described by Klein et al. (2023). A body of stainless steel is glued to the back of the fiber-reinforced plastic part to provide mechanical stiffness.

Six high-power LED systems (HARDsoft IL-105/6X Illuminator UV) illuminated the TSP surface, each of them equipped with a lens system to focus their emission and a low-pass filter having a center wavelength of 385 nm and

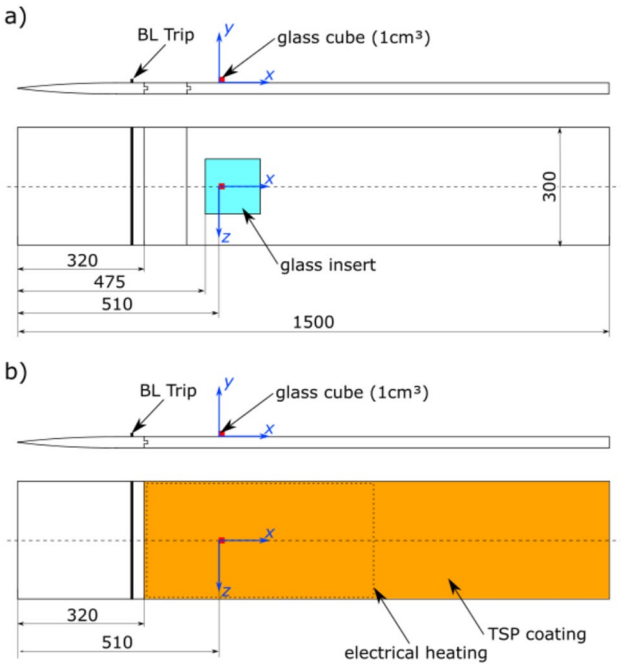

Fig. 2 Experimental setup and coordinate system of the different flat plates for each measurement technique: LPT (**a**) and TSP (**b**)

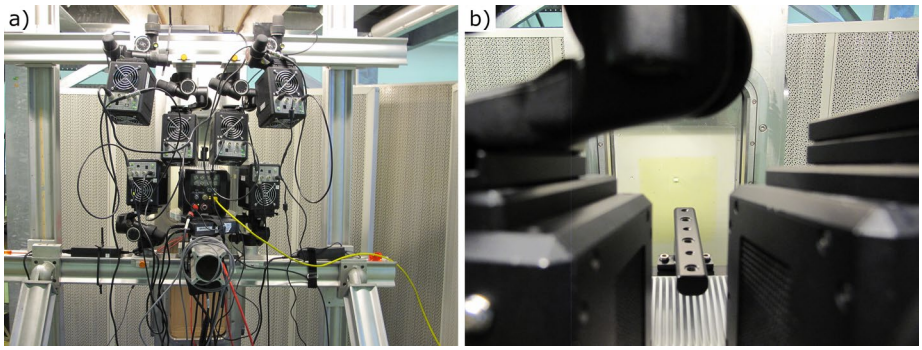

Fig. 3 Experimental setup for the TSP measurement: arrangement of six UV-LEDs for illumination and the high-speed CMOS camera in the bottom center (**a**), glass cube and TSP surface from camera perspective (**b**)

bandwidth of 70 nm. TSP images have been acquired by a monochromatic CMOS high-speed camera (Vision Research v2640) with a resolution of 2048 px × 1952 px, and a bit depth of 12 (Fig. 3a).

The camera was equipped with a 50 mm lens, providing a field of view of 180 mm × 230 mm in streamwise and spanwise direction, respectively (Fig. 3b), A band-pass filter with a central wavelength of 630 nm and a bandwidth of 75 nm minimizes stray light from the illumination.

3D STB partice tracking: Experimental set-up. For the STB LPT measurements, a transparent glass insert of 150 mm × 150 mm is integrated into the splitting plate. The cube is glued to this plate with a refractive index matched glue, which allows a view from behind the plate and ensures minimal reflections of the laser light. The beam of a high-speed laser (Quantronix Darwin Duo) is enlarged and shaped by a passe-partout to a cross section of 80 mm (streamwise) by 20 mm (wall-normal) (see Fig. 4a and b). The expanded

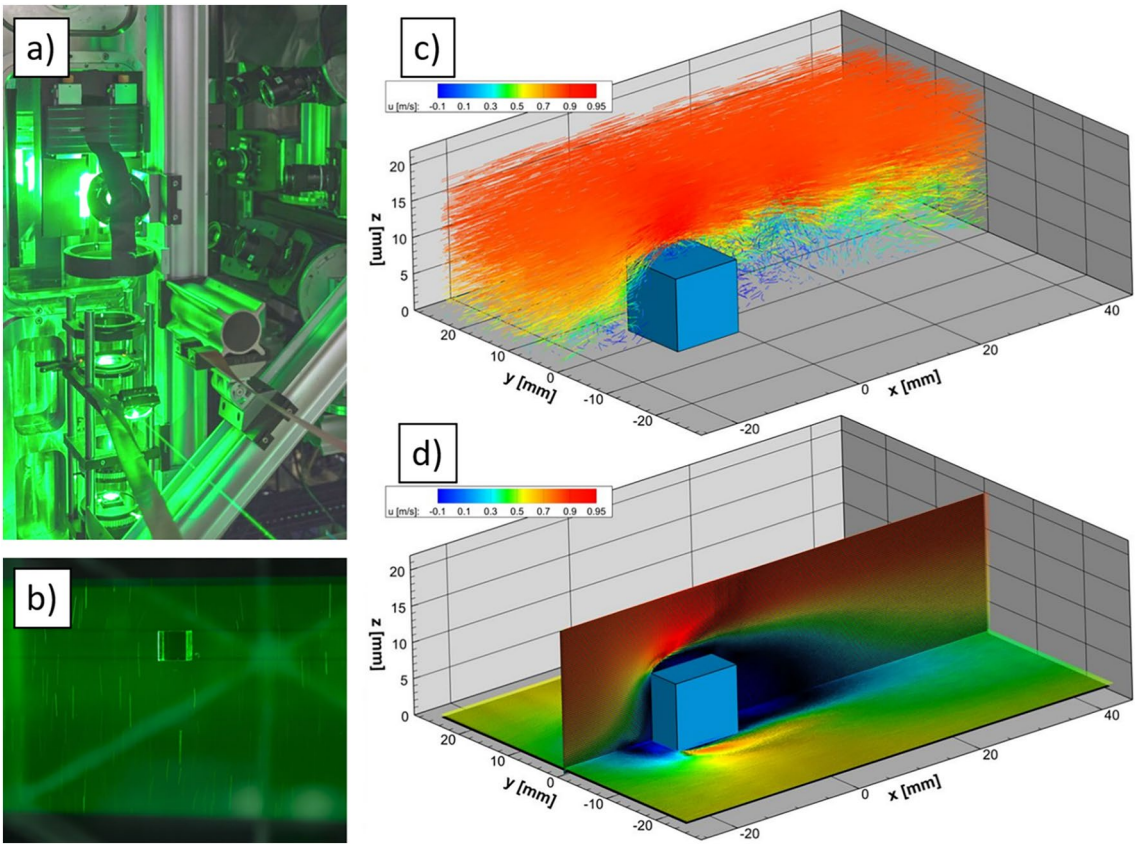

Fig. 4 Experimental setup and from LPT experiment. **a** Laser light volume generation by the high speed laser with camera setup visible in the background. **b** The 1cm^3 cube and single particles around it as traces from multiple illuminations. **c** Tracking result, showing ten consecutive time-steps of approx. 67000 tracked particles at $U_\infty = 0.8\,\mathrm{m\,s^{-1}}$, cut at the cube middle plane. **d** Averaged result, gained by binning all available measurement runs in 0.25 mm^3 bins. Shown are a wall-normal cut at the cube midplane and a wall-parallel cut at $z = 1$ mm

light beam is reflected by a mirror on the opposite side of the tunnel such that it passes the measurement volume a second time, thereby increasing the light intensity and ensuring symmetric scattering toward all cameras. The laser is operated at a repetition rate of 1.5 kHz with a pulse energy of approximately 20 mJ. The water is seeded using polyamide particles (Vestosint) with an average diameter of approximately 30 µm. Unfortunately, the particles were found to be very polydisperse, with sizes ranging from 5 µm to 70 µm. This polydispersion proved to be detrimental to the reconstruction process and limited the attained seeding density.

The illuminated particles are recorded by a system of seven high-speed cameras, operated at the same framing rate of 1.5 kHz. Six PCO Dimax-S4 view the cube through 100 mm lenses (Zeiss-Planar T100/2) from the forward side, looking through a tailor-made six-faced water-filled prism, which allowed each camera a perpendicular view through the air-water interface, thereby minimizing astigmatism effects. These cameras have a common spanwise viewing width of approx. 80 mm at the position of the cube. Another high-speed camera (Phantom Miro 340) is installed on the opposite side of the tunnel and images the immediate vicinity of the cube through both the tunnel window and the glass insert using a 200 mm lens. This camera allows a more robust tracking at the foot of the cube, where the particles are hidden from view for some of the other cameras by the cube itself. For camera calibration a 3D target is placed downstream of the cube and is simultaneously imaged by all cameras. The geometrical calibration is later refined using Volume-Self- and OTF-calibration (Wieneke 2008; Schanz et al. 2013). For more information on the experimental setup and evaluation strategies, as well as results for other velocities at laminar inflow conditions, the reader is referred to Schröder et al. (2020).

2D STB particle tracking: Experimental set-up. A two-dimensional time-resolved measurement was performed on a plane vertical plane along the mid-line (symmetry plane), and extending upstream for a distance of 8 mm from the front face of the cube (see Fig. 5bc). The imaging setup used a macroscopic lens of 100 mm focal length (Zeiss Planar T100/2) at an aperture of f-number 4.0. A high-speed camera with a 4 megapixel CMOS sensor was used (PCO AG, Dimax-S4), which features a pixel pitch of 11 µm or 16.67 µm/pixel in object space. The camera resolution was reduced to 504 px × 1008 px (streamwise and wall-normal, respectively). Illumination consisted of a pair of externally modulated continuous wave lasers (Kvant Laser, SK) with a combined output power of nearly 10 W at a wavelength of 520 nm. See Schröder et al. (2020) for a more detailed description of the setup.

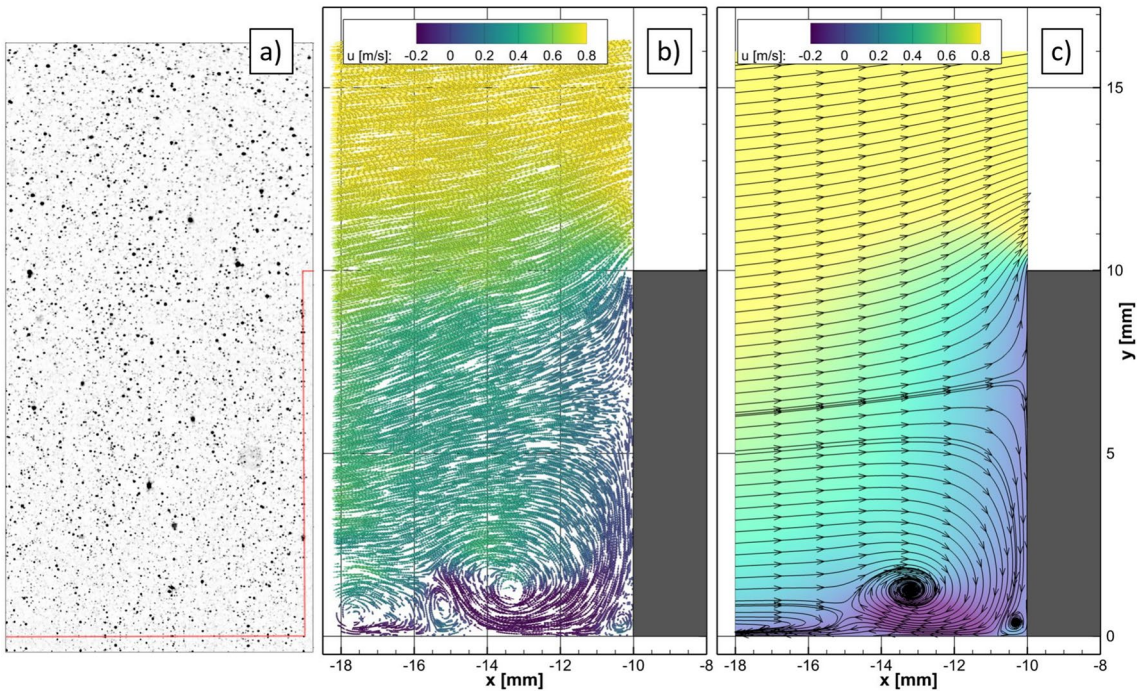

Fig. 5 **a** 2D-2C STB particle tracking in front of the cube. Exemplary preprocessed camera image; position of cube and wall indicated by red lines. **b** Instantaneous result, showing particle tracks for ten consecutive time-steps. **c** Averaged result with streamtraces in 50 × 10 µm resolution

4.2 Data acquisition

TSP experimental conditions: The TSP data were acquired according to the intensity-based method (Liu et al. 2021). This method prescribes acquiring a *wind-off* reference image before acquiring the *wind-on* experimental data. The conditions of the *wind-off* image are characterized by a temperature equilibrium of the model and the fluid. Whereas, a constant heat flux between model and fluid is strived for during the *wind-on* image acquisition to comply with the required boundary condition of the skin friction estimation process in Eq. 9. The following steps were carried out to acquire the *wind-off* images in temperature equilibrium and the *wind-on* images with a near-constant heat flux boundary condition at the wall (Eq. 9) during the measurement:

1. Acquisition of images at reference, i.e., *wind-off*, condition: the fluid temperature was $T_{\text{ref}} = 21.65$ °C, heating system switched off, flow at rest, and LED lamp switched on 5 s before the actual image acquisition. 1000 images were acquired with $F = 100$ Hz with an integration time of $t_{\text{shutter}} = 25$ µs.
2. Switch on the TSP heating system with a heating power of 140 W ($I = 18$ A) and a flow speed of $U_\infty = 0.2\,\text{m s}^{-1}$. After approximately 10 min the heating power was increased to 200 W ($I = 21.5$ A) and the flow speed was increased to the $U_\infty = 0.8\,\text{m s}^{-1}$. After another 6 min of heating the model, the *wind-on* phase was initiated.
3. Acquisition of images at run, i.e., *wind-on*, condition: fluid temperature before the acquisition was $T_{\text{ref}} = 21.76$ °C, heating system still switched on, flow speed of $U_\infty = 0.8\,\text{m s}^{-1}$, and LED lamp switched on 5 s before the actual image acquisition. 6 339 *wind-on* images are acquired with $F = 200$ Hz with an integration time of $t_{\text{shutter}} = 25$ µs.

3D STB experimental conditions: The flow was set to a free stream velocity of $U_\infty = 0.8\,\text{m s}^{-1}$ and was recorded at 1500 Hz for 3675 consecutive images per measurement run. During the tests campaign, a total of 13 runs were performed, yielding a total of 47,775 images. Specific volumetric masks were created for each camera for the region on top of the cube and the cube sides (see Schröder et al. 2020 for details). The algorithm was able to track between 60000 and 70000 particles within each time step. See Fig. 4c for an instantaneous example.

2D STB experimental conditions: The flow was set to a free stream velocity of $U_\infty = 0.8\,\text{m s}^{-1}$ and was recorded at 5000 Hz for two runs of 50373 consecutive images. An exemplary camera image from these sequences is provided in Fig. 5a. The evaluation consisted on applying a 2D-2C version of the STB method (Schröder et al. 2018), yielding around 4800 tracked particles per time-step. Figure 5b reports an instantaneous result, showing the temporally varying system of vortices in front of the cube. It should be noted that the same image data was used in Schröder et al. (2020) but was processed with a cross-correlation-based 2D-2C PIV algorithm.

5 Data preprocessing

5.1 TSP data registration and calibration

The TSP measurement technique records the intensity of the TSP emission in the image reference frame. Thus, several data processing steps are necessary to derive temperature

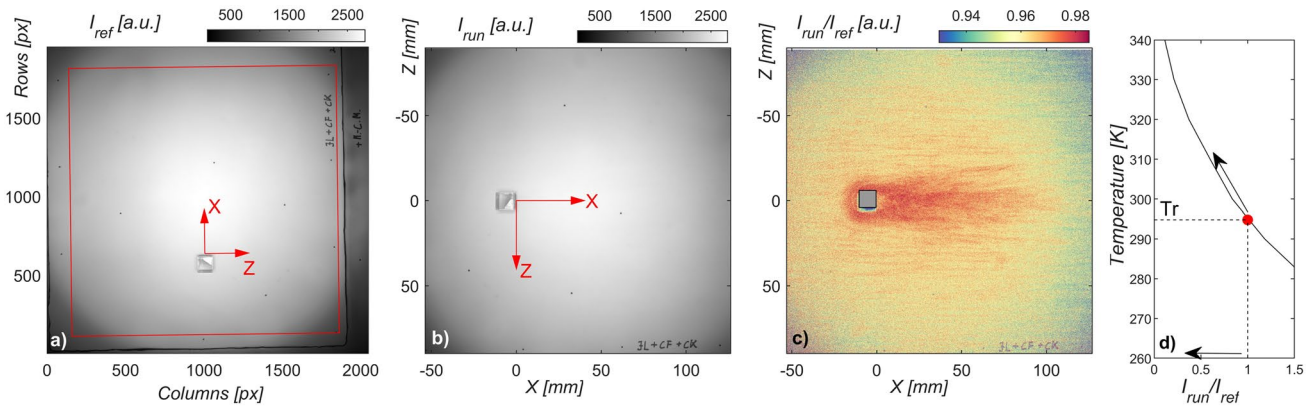

Fig. 6 Logical sequence of temperature map extraction. **a** I_{ref} Wind-off image in the reference system of the CMOS sensor. Black dots at known positions allow rectifying and registering the image space on the final *word* reference frame (in red). **b** I_{run} wind-on image, adjusted of the model's displacement, rectified and registered in the *word* reference frame. **c** Ratio $I_{\text{ref}}/I_{\text{run}}$, always < 1, represented in the *word* reference system. **d** Calibration curve and process: the displacement of the ratio $I_{\text{ref}}/I_{\text{run}}$ from 1, corresponding to the wind-off temperature T_r, identifies the instantaneous temperature for each grid cell

maps on a orthogonal grid with physical dimensions: image rectification, registration onto a structured grid, division of *wind-on* by *wind-off* data, application of temperature calibration, and filtering of the temperature data. Figure 6 provides examples of the steps to derive the temperature in logical order.

Figure 6a shows a raw *wind-off* image in the image reference frame of the camera. The visible intensity distribution is dominated by the illumination pattern and lens effects, which hinders the visibility of the aerodynamic structures. The format of the intensity I_{ref} is an unsigned integer at 16 bits (uint16).

The set of black markers in the TSP coating of the flat plate at known positions allows the definition of a grid with the desired node spacing on an external (*word*) reference system. Then, the *wind-off* image is rectified and registered using the inverse affine mapping that back-projects the markers from the *image* reference frame to their known original position in the *word* reference system. The final 858 × 858 grid has an *a-priori* imposed resolution of $dx \equiv dz = 0.21\,\text{mm}$. The subpixel sampling procedure follows the generalized interpolation guidelines reported in Thévenaz et al. (2000) using a fifth-order B-spline.

During experiments, the camera-model system could undergo unwanted relative movements that require correction. For each *wind-on* image, the inquiry about the displacement of the same set of dot-like markers from its original position allows checking the occurrence of unwanted displacements. Then, the *wind-on* images are rectified and registered using the same procedure as for the *wind-off* images. Figure 6b reports one of the *wind-on* images after image registration onto the structured grid on the *word* reference system as the red rectangle in Fig. 6a. The image intensity I_{run} is still in uint16 format.

The transformation of the measured intensities into the temperature map shown in Fig. 6c requires a calibration of the TSP coating. The procedure relies on a calibration curve, as shown in Fig. 6d, describing the intensity evolution of the emission of a coating sample as a function of the sample temperature under carefully controlled steady excitement conditions (Egami et al. 2009). To compare the emission intensity of the *wind-on* image against that in the generic calibration curve, both quantities are normalized by the emission of the paint at the *wind-off* reference temperature T_r. The *wind-on* image intensity I_{run} is ratioed by the 2D *wind-off* emission map I_{ref} (see Fig. 6c), while the emission axis in the calibration curve is ratioed by the scalar representing the sample emission at reference temperature T_r on the calibration curve itself (see Fig. 6d).

A first glance feasibility of the $I_{\text{run}}/I_{\text{ref}}$ ratio in minimizing unwanted disturbances is given by comparing the structure of the image intensity in Figs. 6a and b against 6c. The first two figures retain the spot-like light shape distribution existing on the experimental setup. Their ratio in Fig. 6c minimizes the non-uniform lighting. Fine details of coherent structures in the flow became visible, although embedded in the signal's noise. It is worth noticing the data format in Fig. 6c is a 32 bit floating point one.

5.1.1 TSP filtering

The recent availability of high-quality CMOS sensors expanded the limits of luminescence-based imaging. Their low noise and fast time readout allow for reducing the minimum light required to capture image sequences at a very high frame rate. However, the original CMOS design strategy establishes that each pixel acts as an individual device with its charge-voltage conversion, according to its gain and offset. Combined with the extra noise source due to the TSP coating luminescence, the final measurement results are far from an ideal fast and quantitative imaging system (see Mandracchia et al. 2020 and references within). To address this issue, the calibrated and registered temperature data have been filtered in space and time, with special care in preserving edges in the space domain and spectral behavior in the frequency domain.

Space filtering (SG): The edge-preserving spatial filtering described in Miozzi et al. (2019) is adopted here to preserve the temperature gradients within instantaneous images while removing the uncorrelated, white noise in the background. The method modifies the classical Gaussian smoothing technique by squeezing the Gaussian bell according to the local temperature gradients. Based on the eigenvalues $\lambda_{1,2}$ and eigenvectors $\Psi_{1,2}$ of the intensity gradients correlation matrix calculated on the 9 px × 9 px window surrounding each pixel, the circular shape of the Gaussian bell is squeezed in the direction retaining the maximum of the energy (eigenvector Ψ_1 with eigenvalue λ_1). The axes of the resulting ellipse along Ψ_2 and Ψ_1 are in the same ratio as $\lambda_1/\lambda_2 > 1$, limited to 1.5 to avoid numerical degenerations. All TSP maps are convolved with the Gaussian-like kernel:

$$G(x,y) = e^{-\left(\frac{(x\cos\theta+y\sin\theta)^2+\gamma^2(-x\sin\theta+y\cos\theta)^2}{2\sigma^2}\right)} \tag{13}$$

where θ is the orientation of Ψ_1, $\gamma = \lambda_1/\lambda_2$ is the aspect ratio, and σ is the Gaussian kernel's standard deviation, which modulates the smoothing intensity. This enhanced version of the classical Gaussian blur (Koenderink 1984) smooths the image where the data exhibit a spatially coherent gradient by applying a weak stretch of the kernel normal to the gradient itself, limiting the smoothing of meaningful edges.

Time filtering (SPOD): Images capturing the intensity of the emission of luminescent materials are prone to noise induced by several factors. Here, the temperature measurement by TSP adopts the *intensity* method,

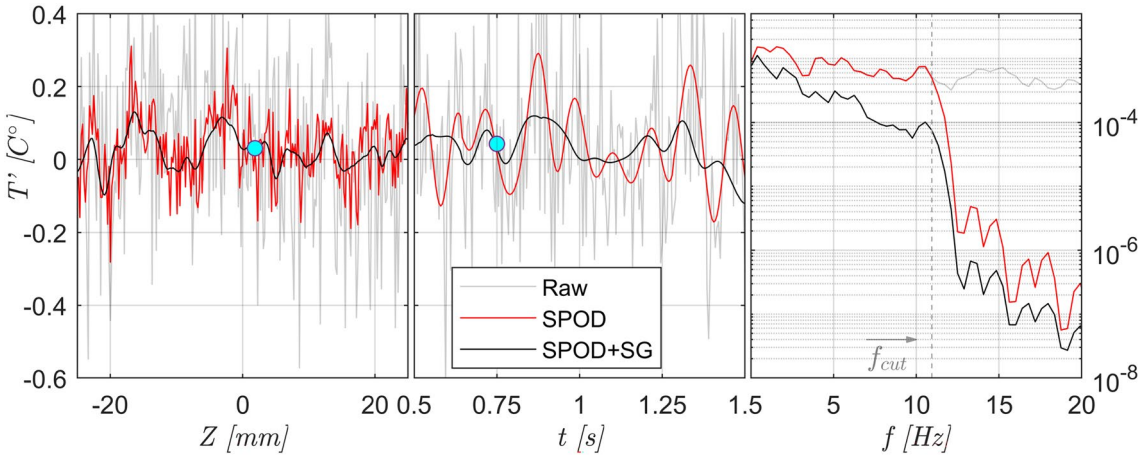

Fig. 7 Comparison between raw (gray lines) and data filtered in time (SPOD, red lines) and space (SPOD+SG, black lines). **a** Spatial profiles of T' along Z (dashed section in Fig. 8a) at time 0.75 s (cyan marker in Fig. 7b). **b** Detail of a time history of T' at $X = 1.89$, $Z = -4.91$ (cyan marker in Figs. 7a and 8abc). **c** Power spectral density (PSD) of the three time histories in Fig. 7b

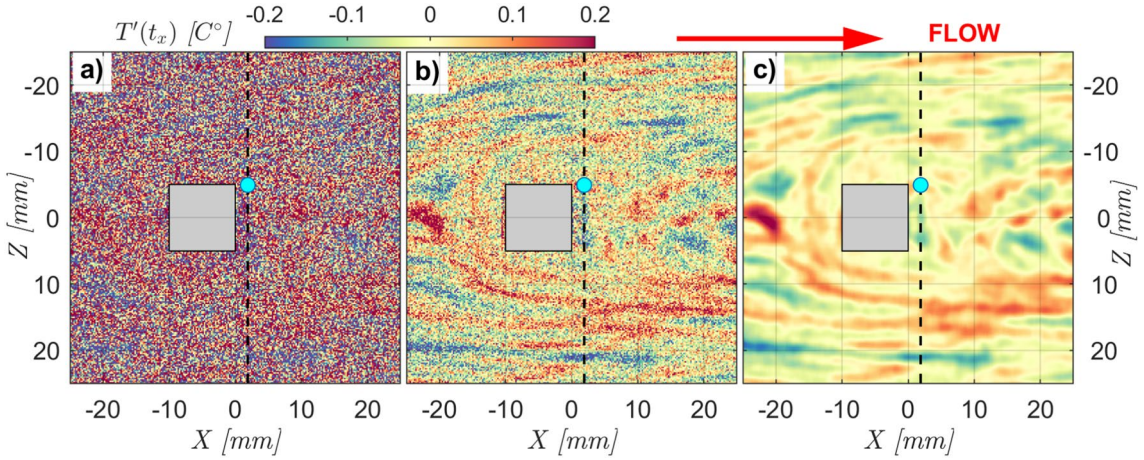

Fig. 8 Comparison of $T'(t)$ maps at $t_x = 0.7$s among **a** unfiltered data, **b** data filtered in time (SPOD) and **c** data filtered in time and space (SPOD+SG)

assuming a steady condition of the exciting radiation. While the wind-on/wind-off ratio effectively minimizes the spatial inhomogeneities of the TSP emission, the lack of *wind-on* steadiness is hard to recover. From this perspective, the presence of impurities in the fluid (i.e. residual seeding of previous PIV tests, rust, micro-algae, etc.) operates as a partial or total screen in the light path between the LED excitation source and the TSP surface, and from the emitting TSP surface to the CMOS sensor. The fluid running in the test section for the present TSP experiment was contaminated by impurities projecting fake shadows on TSP images, running as fast as the outer velocity. They jeopardize the measurement's quality and must be suppressed or minimized. To this aim, the time history of T at each pixel was low-pass filtered below $f_{\text{cut}} = 10.93$ Hz following the method based on the Spectral POD Decomposition (SPOD) described in Nekkanti and Schmidt (2021), which allows reconstructing the original signal with previously defined cutting frequency f_{cut} and with limited artifacts in the spectral domain.

Figure 7a, b shows the modifications that temporal and spatial filters induce on the original data, more specifically on a spatial $T'(x_0, z, t_x)$ and temporal $T'(x_0, z_0, t)$ profile. Filtering acts in two successive steps. Firstly, the energy of the raw, noisy data (gray line) is drastically attenuated above $f_{\text{cut}} = 10.93$ Hz by the low-pass SPOD filtering (red line). Then, the SG filter cut out the residual spatial fluctuations of T' associated with high wave numbers. Spectral analysis in Fig. 7c shows the low-passing action of the SPOD filter on the original signal (red line). The successive SG filter (acting in space) reduces the signal energy without introducing artifacts. Figure 8 illustrates

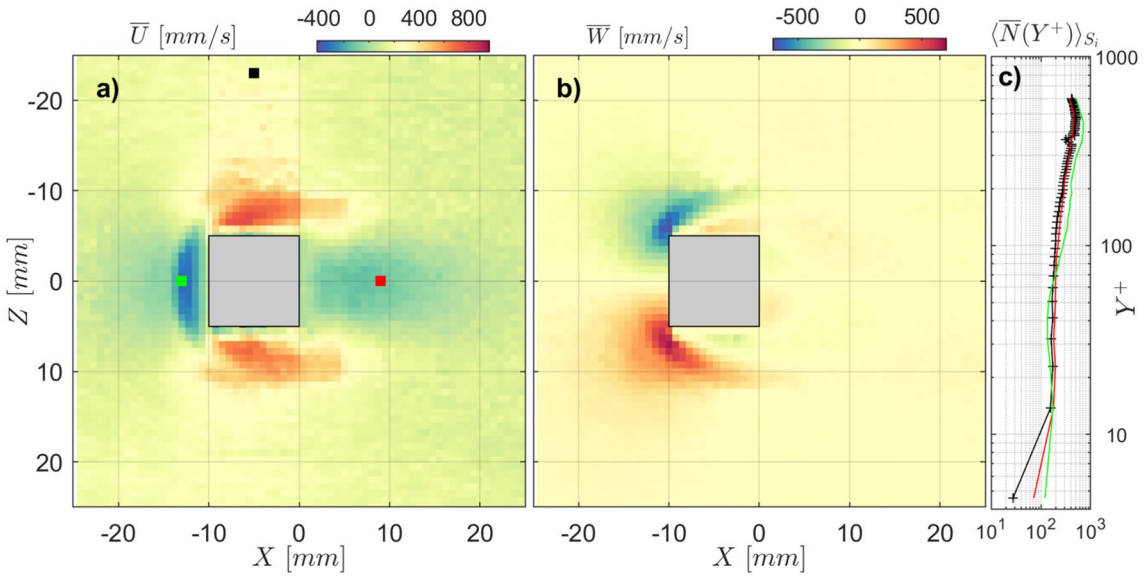

Fig. 9 **a** Map of $\overline{U}$ at $Y^+ = 2.7$, **b** map of $\overline{W}$ at $Y^+ = 2.7$. **c** number of particle trajectories $\overline{N}$ averaged over the three small regions S_i, black, red, and green, reported in the map alongside

the overall filtering contribution to the signal clearness: the almost unintelligible $T'(x, z, t_x)$ map in Fig. 8a reveals, after SPOD filtering, the pattern of the flow surrounding the cylinder. SG filtering removes the small spatial scales and, at the same time, strongly influences temporal scales as well (Fig. 8c).

5.2 STB time-averaged data binning and smoothing

The results of all time steps for all 13 runs of the 3D measurement were obtained by dividing the volume in a grid of small bins and averaging for each bin the properties of all particles at any time located within it. Two different dimensions of the binning array will be used within this manuscript: Cubic bins with a side length of 0.25 mm $\approx 9.2Y^+$, guarantee to retain a high and isotropic spatial resolution in the flow, which is most suitable for visualizations (see Figs. 4d and 15). With such a bin size, the first node extends to $\approx 4.6Y^+$, close to the outer edge of the viscous sublayer. Therefore a second $104 \times 94 \times 134$ grid, with a spatial resolution of $dx = dz = 0.75$ mm $\approx 27.6Y^+$ and $dy = 0.15$ mm $\approx 5.5Y^+$, was adopted for the wall-normal derivative, which puts the center of the first node at $\approx 2.7Y^+$ (≈ 0.075 mm) and enlarges the horizontal bin size. This approach returns good time-averaged statistics, with an acceptable loss in spatial resolution. Figure 9a and b reports planes of the streamwise and spanwise velocity components at the first node, respectively.

Figure 9c describes the number of reconstructed trajectories $\overline{N}(Y^+)$ that are found to be located at increasing distances from the wall. Three wall-normal profiles illustrate the evolution of the available tracked particle statistics with the wall distance at three different locations placed upstream, downstream, and spanwise of the cube (green, red, and black squares in Fig. 9a). The lower concentration of trajectories in the regions close to the surface might be attributed to a restricted illumination close to the wall and a drop of the available particles. An even more significant drop of tracked particles in the grid node closest to the surface is visible on both sides of the cube (Fig. 9a), due to the back-reflected laser sheet. Its effect is less pronounced higher up in the volume; we suspect that the glue used for fixing the cube led to shadowing effects of the coherent light. Another possible cause for reduced particle density close to the wall might be the integrated Magnus effects due to the comparatively large size of the seeding particles relative to the viscous length, though this was not observed for the 2D case.

The averaged 2D data was obtained by dividing the measurement area in small bins of 50 µm ×10 µm and averaging all particles located inside each bin throughout the available 2×50307 time-steps. Each bin is populated by 2000 to 3000 particles. See Fig. 5c for an image visualizing the streamwise velocity component and streamlines of the averaged result.

5.3 2D STB time-resolved Natural Neighbors interpolation

The 2D STB time-resolved Lagrangian snapshots, acquired at a high particle density, are used to get an Eulerian flow representation at each measured time step. To this aim, each

instantaneous dataset is interpolated following the Natural Neighbor (NN) approach (Sibson 1981; Miozzi 2005). In the classical approximation schemes, the search for the data supporting a grid node is usually isotropic (circular in 2-D), non-negative within a circle of some fixed radius. The weight of each point monotonically decreases with distance from the querying point P. As an implicit assumption, nodes closer to P contribute with a larger weight to the interpolated value on P than those at greater distance. On the contrary, in NN interpolation the support for data gridding is not defined by the same measure in all directions but is allowed to be non-isotropic. The support size in any direction r is not given by an L_2 metric but is a consequence of the geometric construction of the networks, which locally defines the region of interaction between features.

The NN interpolation is based on the Delaunay Triangulation (DT), and its dual, the Voronoi Tessellation (VT) built on the instantaneous snapshot nodes. The DT is a unique triangulation that connects all the measured Lagrangian nodes. Its construction must comply with the *empty circumcircle* concept: each circle passing for the three vertexes of each triangle has to be empty, i.e. no other node can fall within it. The dual of DT, the VT, is a unique tessellation built by connecting the axes of the sides of each triangle in DT. Figure 10a reports the dual networks with lighter (DT) and darker (VT) edges. This dual representation supports the NN interpolation.

The basic expression of the NN is:

$$F(x,y) = \sum_{i=1}^{N} \phi_i(x,y) \cdot f_i(x_i,y_i) \tag{14}$$

where $F(x, y)$ is the interpolated value at $P \equiv (x, y)$ location, $\phi_i(x, y)$ is the weight function and $f_i(x_i, y_i)$ are the known data at $P_i \equiv (x_i, y_i)$ position.

When a grid point P queries for its interpolated value it is inserted in the network, disrupting the *empty circumcircle* state of a specific set of nodes P_i. This set of nodes constitutes the NN support ($\otimes$ points in Fig. 10) that provides the grid value by their weighted contribution ϕ. Here, without loose of generalities, we will use the classical Sibson approach (Sibson 1981). It grounds on the observation that the insertion of the grid point P modifies also the VT of each P_i, giving rise to a new polygon (thick black perimeter in Fig. 10). The overlap degree of the new polygon with the preexisting tessellation (colored patches in Fig. 10 left) defines the NN shape function $\phi_i(x, y)$ for each node P_i in the NN set. Formally, the weight functions are defined as:

$$\phi_i(x,y) = \frac{A(x_i,y_i)}{A(x,y))} \tag{15}$$

where $A(x, y)$ is the surface of the new polygon centered in P, and $A(x_i, y_i)$ is the intersection between the new polygon centered in $P(x, y)$ and the old polygon centered in $P_i(x_i, y_i)$.

Two representative shape functions, with unitary value at the apex, are reported in Fig. 10 right. The NN interpolation generates a surface of class C^1 except at the NN sparse nodes location, where the interpolation guarantees the reply of the original value. The no-slip condition at the wall is forced by mirroring the original sparse dataset (green points) around the $Y = 0$ axis and changing the sign of the associated fluid dynamic quantities (red points).

6 Results and discussion

Table 1 reports the parameters of the incoming, still undisturbed boundary layer at upstream position $x = -52$ mm, as reported in Schröder et al. (2020). In the following, quantities in wall units refer to the viscous length specified in Table 1.

As a preparatory step, this section begins with two subsections concerning the outcomes of the NN interpolation algorithm applied to the 2D STB data. The former reports a sensitivity analysis of the wall distance influence on the wall shear stress evaluated by the wall-normal derivative ($\tau_{X_{V_{NN_{WN}}}}$, shortly τ_{X_V} unless there is ambiguity). The latter investigates the magnitude of the c_U parameter in Eq. 1. The c_U estimation obtained so far is then modulated by the c_T coefficient (Hetsroni et al. 2004) and applied to the extraction of $\overline{\boldsymbol{\tau}}_T$. Topology and magnitude of the wall-shear stress $\overline{\boldsymbol{\tau}}_T$ and $\overline{\boldsymbol{\tau}}_V$ are then compared and commented on in the remaining subsections.

6.1 Sensitivity of the instantaneous wall-shear stress from the wall-distance

The six wall shear stress probability maps $P(\tau_X(X,t)|X)$ in Fig. 11a–f emphasize the streamwise evolution of τ_X dispersion around $\overline{\tau_X}$. Regions of larger dispersion correspond to the near-wall coherent structures visible in Fig. 5b. The variations induced by increasing the wall distance are visible for $Y^+ > 3$ and affect mainly the tails of the probability curve. The profiles $P(\tau_X(X,t)|X_0)$ in Fig. 11g illustrate the influence of Y^+ on the probability extracted at section $X_0 = -13$ mm. Below $Y^+ = 3.415$ the profiles show only marginal deviations. At that distance and above, the distribution loses its skewed feature, and its shape becomes increasingly symmetric. Notwithstanding the evidence of these tails' variation on the PDF profiles, the time average of the wall shear stress remains almost unchanged at increasing wall distance

Table 1 Characteristic parameters of the boundary layer at upstream position, $x = -52$ mm (Schröder et al. 2020)

Flow condition		Turbulent
Reynolds number Re_H		8000
Tunnel setting U_∞	[m/s]	0.8
Measured U_e	[m/s]	0.829
BL thickness, δ_{99}	[mm]	11.29
δ/H	–	1.13
Displacement thickness, δ^*	[mm]	1.79
Momentum thickness, θ	[mm]	1.24
Shape factor, δ^*/θ	–	1.45
Friction coefficient, c_f	–	0.00417
Mean wall shear rate, $dU/dy\|_{y=0}$	[1/s]	1394
Estimated wall shear rate	[1/s]	1430
Shear rate integral $\int_0^\infty (dU^*/dy^*)\, dy^*$	–	0.978
Estimated friction velocity, u_τ	[m/s]	0.0389
Viscous length, $y^+ = \nu/U_\tau$	[μ m]	27.2
Viscous length in image space	[px]	1.6
I^{st} grid cell size (v.u.) $\Delta \boldsymbol{X}^+ = \Delta \boldsymbol{X}/y^+$	–	9.2
I^{st} grid first node (v.u.) $Y_0^+ = 0.5 \cdot \Delta Y/y^+$	–	4.6
II^{st} grid cell size (v.u.) $\Delta \boldsymbol{X}^+ = \Delta \boldsymbol{X}/y^+$	–	[27.6 5.5 27.6]
II^{st} grid first node (v.u.) $Y_0^+ = 0.5 \cdot \Delta Y/y^+$	–	2.7
$Re_H = U_\infty H/\nu$	–	7820
$Re_\delta = U_\infty \delta_{99}/\nu$	–	8830
$Re_\theta = U_\infty \theta/\nu$	–	996
$Re_\tau = U_\tau \delta_{99}/\nu$	–	415

(Fig. 11g), while the standard deviation is weakly affected by the changes.

6.2 Linking the friction velocity and the celerity of disturbances

The 2D STB dataset consists of a high-density Lagrangian description of the velocity field close to the wall, just upstream of the front side of the obstacle. The Eulerian time-averaged flow velocity dataset obtained after the Lagrangian data binning operation (Sect. 5.2) allows computing the friction velocity through the wall-normal derivative $u_{\tau_{V_{WN}}}$ from Eq. 12.

The application of the TH algorithm (Eq. 5) to the Eulerian time-resolved dataset obtained after the interpolation of the Lagrangian data with the NN approach makes available the time-averaged celerity of velocity fluctuations $U_{U_{V_{TH}}}$ and allows to extract the c_U coefficient as the one providing the best overlap between $u_{\tau_{V_{WN}}}$ and $u_{\tau_{V_{TH}}}$.

Figure 12 compares different estimations of $\overline{u}_\tau$ along the middle line $Z = 0$, from both 3D and 2D STB. The u_τ profile from 3D data (continuous black line, squares) slightly exceeds the estimations coming from the 2D ones. These latter are evaluated by applying the wall-normal derivative operator to both the bin-averaged dataset (continuous blue line, circles) and the time-average field obtained from the NN time-resolved snapshots (dashed red line, crosses). These last two series completely overlap, as a confirmation of the effectiveness of the NN interpolation.

Focusing on the comparison between the $\overline{u}_{\tau_V}$ outcomes from the wall-normal derivative and the one from the TH algorithm, the green continuous line in Figs. 12 represents $\overline{u}_{\tau_{V_{TH}}} = \overline{U}_U/c_U$, where $c_U = 1.667$ is a best fitting estimation. The detail reported in Fig. 12 left shows how, close to the cube, $\overline{u}_{\tau_{V_{TH}}}$ exactly overlaps $\overline{u}_{\tau_{V_{WN}}}$ and remains acceptable all over the range of 2D STB data availability, with a spike-like exception at larger negative values around $X = -13$ mm.

This picture puts together results derived only from velocity data, in a region where the surrounding conditions evolve downstream from adverse to favorable and again to adverse pressure gradient. Having in mind the questions about the nature of c_U, the excellent overlap between $\overline{u}_{\tau_{V_{TH}}}$ and $\overline{u}_{\tau_{V_{WN}}}$ is a clue of a weak dependence (if any) of c_U to the local pressure gradient. The large magnitude difference compared to that reported in the literature for TBL ZPG and APG ($c_U \approx 10$, see Kim and Hussain 1993; Geng et al. 2015, among the others) suggests a dependency on the Reynolds number which is worth further investigation, but is out of the scope of the present work.

The information on c_U obtained so far is adopted for u_{τ_T} estimation from the temperature fluctuations (Eq. 7). Assuming a constant heat flux as the thermal boundary condition, the discrepancy between viscous and thermal diffusion is modulated by $Pr^{-0.5}$ (Eq. 9). The outcomes from TSP on the middle plane are shown in Fig. 12 right, for an extended streamwise range. The figure reports $\overline{U}_{\tau_T}$ as a crimson continuous line and compares it against data from 3D STB. In front of the cube ($X < -10$ mm), $\overline{U}_{\tau_T}$ doesn't capture the footprint of the horseshoe vortex at the wall, and speculations about this will be discussed in the following. Behind the cube, the profile of $\overline{U}_{\tau_T}$ shows a general agreement with the one extracted from 3D STB data and the wall-normal derivative, which will be explored further below.

6.3 Celerity of propagation of temperature fluctuations

Figures 13a, b reports $\overline{\boldsymbol{U}}_\tau$ extracted using the TH algorithm. Streamwise and spanwise components range between – 50 to 100 mm s^{-1} and – 50 to 50 mm s^{-1}, respectively. Spatial resolution is 0.21 mm/px. The pictures report the ROIs of the 3D STB measurement (dashed line) and that adopted in the topological analysis to be discussed in Sect. 6.4 (dash-dot

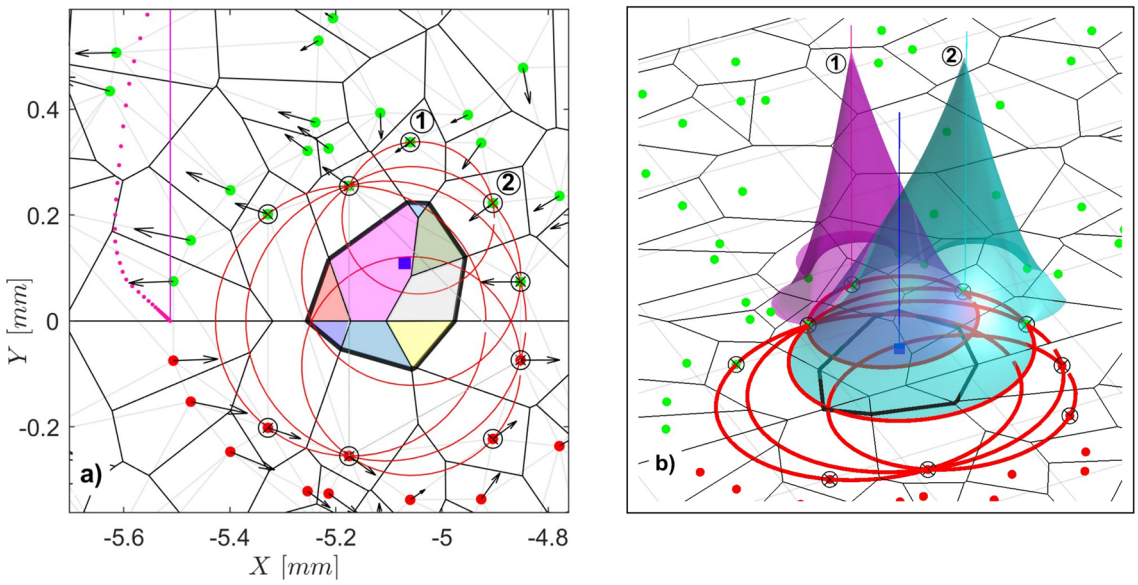

Fig. 10 **a** NN identification (⊗ green and red points) by looking for the circumcircles (red circles) breaking the "empty state" rule after the grid point insertion (blue square). The crimson dotted line reports one vertical profile of the streamwise velocity component. The adjacent solid line marks the profile's location and its $U = 0$ axis, confirming sparse data replication (the head of the lower vector falls on the crimson dotted line) and no-slip condition (zero crossing at the wall). See text for further comments. **b** shape functions (weights) of the topmost NN and its right side neighbor in the alongside picture, identified by the circled numbers 1 and 2

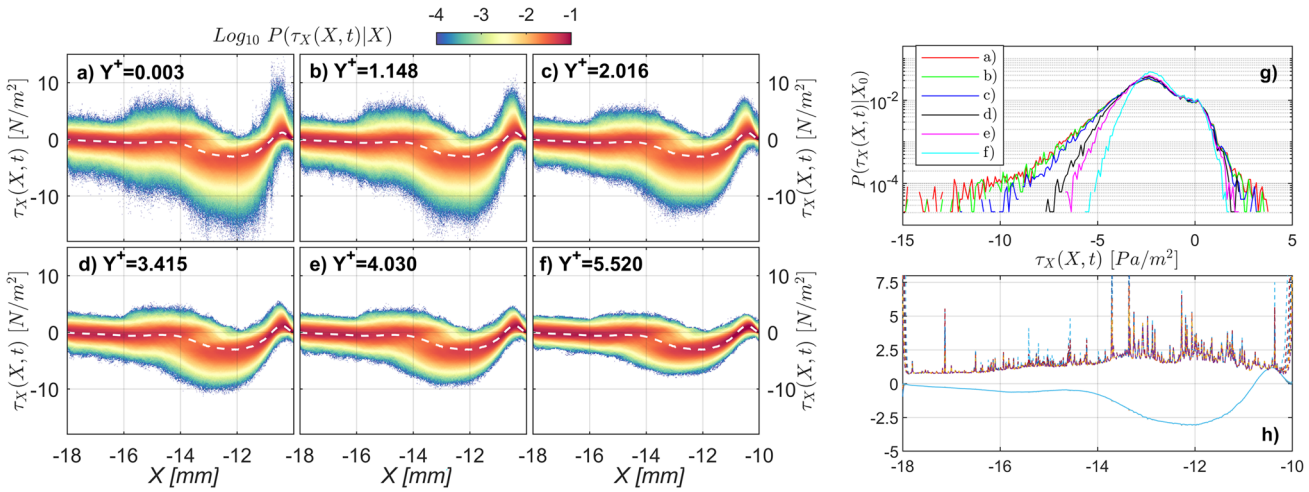

Fig. 11 Sensitivity of $\tau_{X_{V_{NN_{WN}}}}(X,t) \approx \mu \Delta U(X, Y_i, t)/\Delta Y_i$ on the wall distance Y^+. **a–f** Wall shear stress probability maps $P(\tau_{X_V}(X,t)|X)$ extracted at six Y^+ wall distances, overlapped by $\overline{\tau}_{X_V}(X)$ (white, dashed line). **g** Probability profile of wall shear stress $P(\tau_{X_V}(X,t)|X_0)$ extracted at section $X_0 = -13$ mm for the same six Y^+ wall distances. **h** Streamwise time average and standard deviation profiles $\overline{\tau}_{X_V}$ and $\sigma(\tau_{X_V})$ of the wall shear stress at the same six Y^+ wall distances. The six time-averaged profiles collapse on each other and are indistinguishable

line). Their extension underlines how the proposed TSP-based approach makes available information about $\overline{\boldsymbol{\tau}}$ highly resolved in space and time, both around the cube and on wider areas with a relatively simple acquisition system, setup, calibration, and data analysis.

Following Kim and Hussain (1993) and Geng et al. (2015) among the others, the constant c_u in Eq. 1 has been

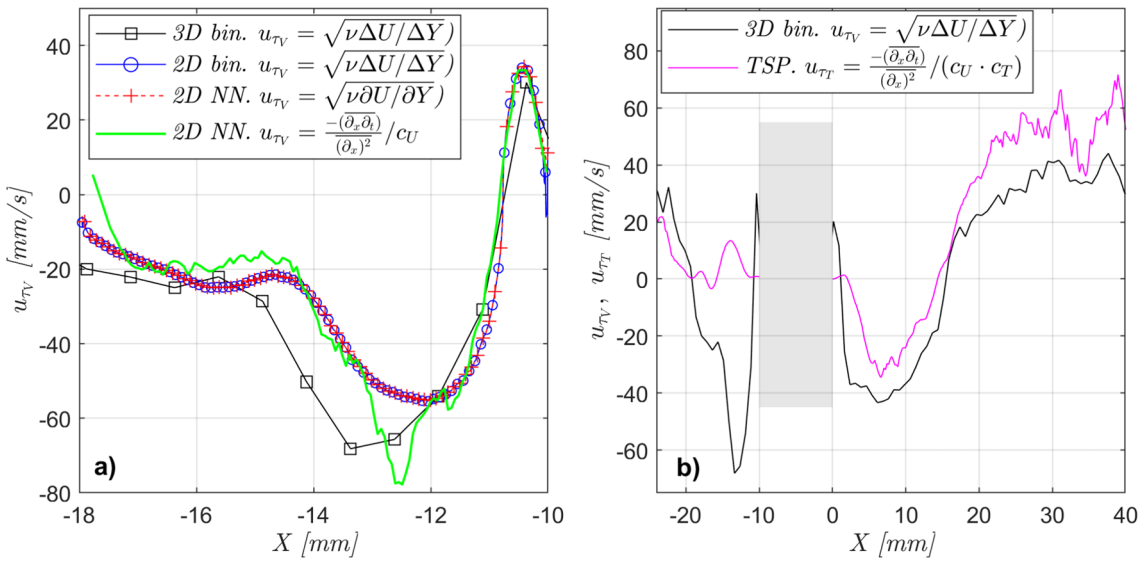

Fig. 12 Friction velocity's streamwise component u_{τ_V} close to the front side of the cube along the cube centerline ($z = 0$), estimated with different methods. **a** detail of the u_{τ_V} profiles. Black, blue, and dashed red lines report the wall-normal derivative of the streamwise component. The green line reports $\overline{U}_U/c_U$, where $\overline{U}_U$ is the celerity of propagation of the velocity disturbances coming from the TH algorithm applied to $U(\boldsymbol{X}, t)$, and $c_U = 1.667$. **b** u_{τ_V} profile from 3D STB data compared to u_{τ_T} profile over a wider streamwise interval. The crimson line reports $\overline{U}_T/(c_U \cdot c_T)$, where $\overline{U}_T$ is the celerity of propagation of the temperature disturbances coming from the TH algorithm applied to $T(\boldsymbol{X}, t)$, $c_U = 1.667$ and $c_T = Pr^{-1/2}$

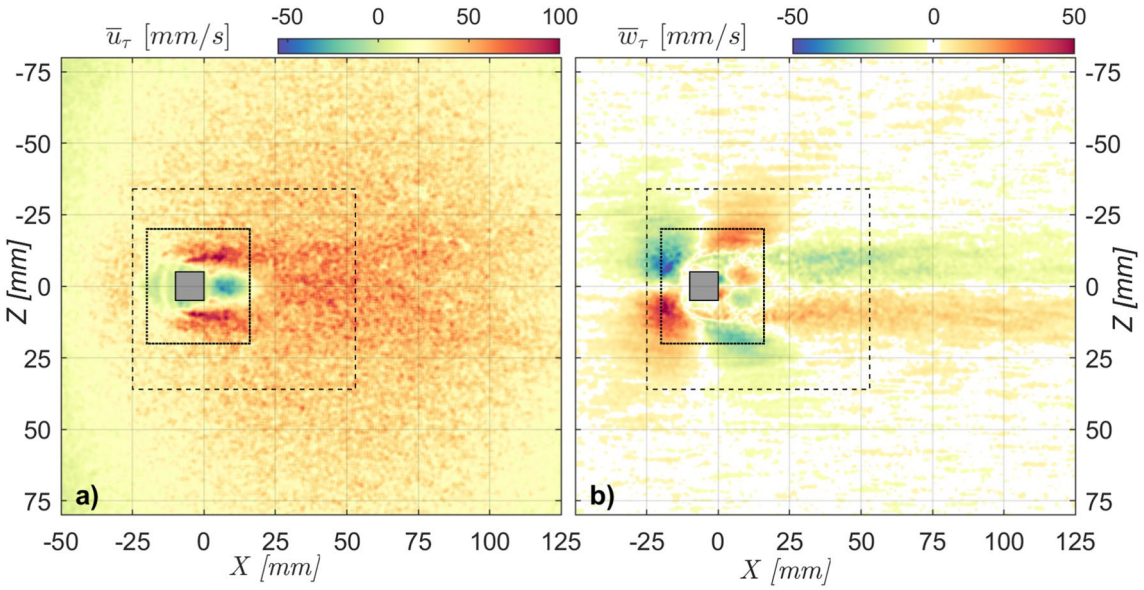

Fig. 13 Streamwise and spanwise components of $\overline{\boldsymbol{U}}_{\tau_T}$ extracted from temperature data. The ROI of the 3D STB measurement is marked by the dashed edges rectangle, while dash-dot edges delimit the ROI of the topological comparison reported later in Sect. 6.4

expected in the range $c_u = 9 \div 10$ for turbulent boundary layers and channel flows, but the scientific literature in the field lacks experiments devoted to its estimation in different conditions.

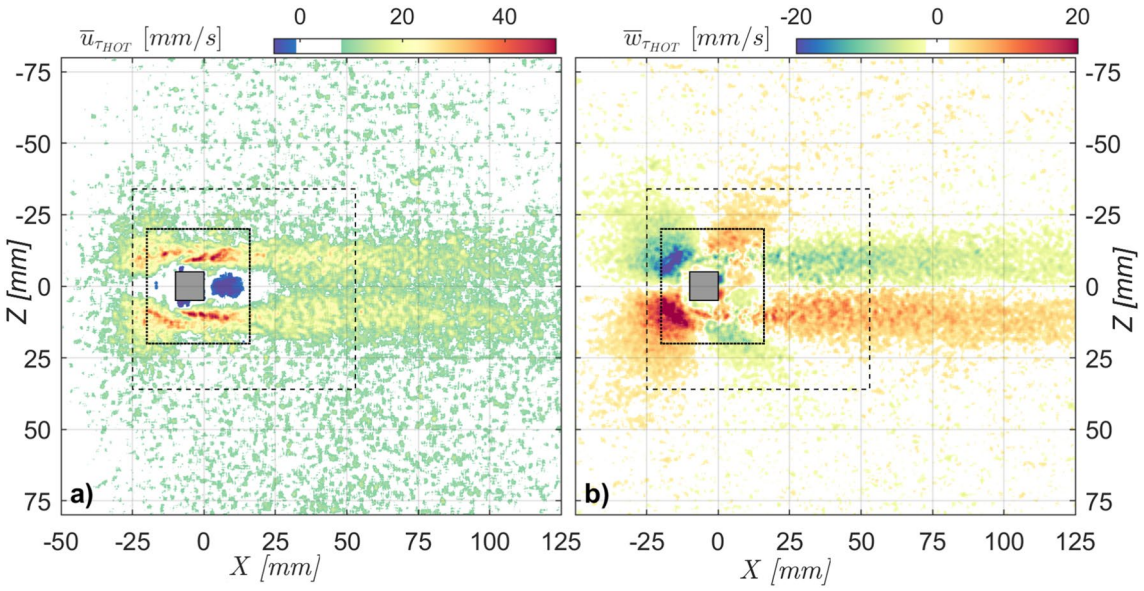

Fig. 14 Spatial distribution and quantification of the higher-order term for **a** $\overline{U}_{\tau_T}$ and **b** $\overline{W}_{\tau_T}$ obtained by subtraction of the simplified estimation in Eq. 5 from the full one in Eq. 4. The magnitude of the higher-order terms reaches about 50% of the $\overline{\boldsymbol{U}}_{\tau_T}$ components reported in Fig. 13

Based on Eq. 9 and the work of Hetsroni et al. (2004) (Sect. 3.1.3), $\boldsymbol{U}_T$ is evaluated by assuming a constant heat flux as boundary condition at the wall (Eq. 9).

6.3.1 The contribution of the higher-order term

The relaxed form of the Taylor Hypothesis here adopted includes a higher-order contribution that introduces a two-components corrective term (Higher Order Term, HOT) based on the correlation between the derivatives of the scalar T along the two axes (Eq. 4). Figure 14a, b illustrates the magnitude and the location of the HOT for $\overline{U}_{\tau_T}$ and $\overline{W}_{\tau_T}$, respectively, obtained by subtraction of the terms in Eq. 5 from these in Eq. 4. To better localize the presence of the correction, maps in Fig. 14 having values lower than 15% of $\overline{u}_{T_{\mathrm{HOT}}}|_{\max}$ (a) or 4% of $\overline{v}_{T_{\mathrm{HOT}}}$ (b) of their maxima have been blanked.

The resulting picture illustrates how the HOT concentrates in regions of upward turning and concentration of wall-parallel vortex lines as they approach the focus point (the arch-shaped vortex roots) or where the helicity is not negligible, i.e. where the wall-tangent vorticity is aligned to the local velocity. In the present test case, both components reach up to 50% of their maxima. It is worth noticing the negative contribution to $\overline{u}_\tau$ within the wake, strictly concentrated at the base of the arch-shaped vortex.

These results state that the high-order term adjustment in Eqs. 4 is mandatory for the correctness of the TH algorithm outcomes, and for the use of the relaxed form of the *frozen turbulence* condition in complex flows.

It is noticed that the inference of U_U from 2D STB data by using Eq. 5 occurs on the middle plane $Z = 0$ where the effect of the higher-order term is minimal, due to the symmetry condition.

6.4 Topological comparison

The analysis of the topological similarities shared by the two flows compares their essential components represented by the nature, spatial location, and connecting manifolds of critical points.

Figure 15 reports the general outline of the time-averaged spatial distribution of the horseshoe vortex system obtained by the 3D STB data. The sketch of the iso-surface $\lambda_2 = -0.00075$ (Jeong and Hussain 1995) illustrates the 3D development of rotational, horseshoe-shaped structures upstream of the cube. Streamlines in the symmetry plane above the top side of the cube report the trip of a rotational region on it. On the rear side, they capture the rotation of the arch-like vortex at its apex. The saddle point S_3 far downstream marks the reattachment of the flow on the middle plane, where also the branches of the separation bubble at the wall around the obstacle converge. Its diverging manifolds head upstream and downstream at the wall, along the $Z = 0$ axes. The upstream manifold marks the middle line between the foci F_1 and F_2, which are the footprints of the arch-like vortex.

The following discussion is organized by analyzing the skin friction results at the front, side, and rear cube sides sectors separately, based on the information sketched in

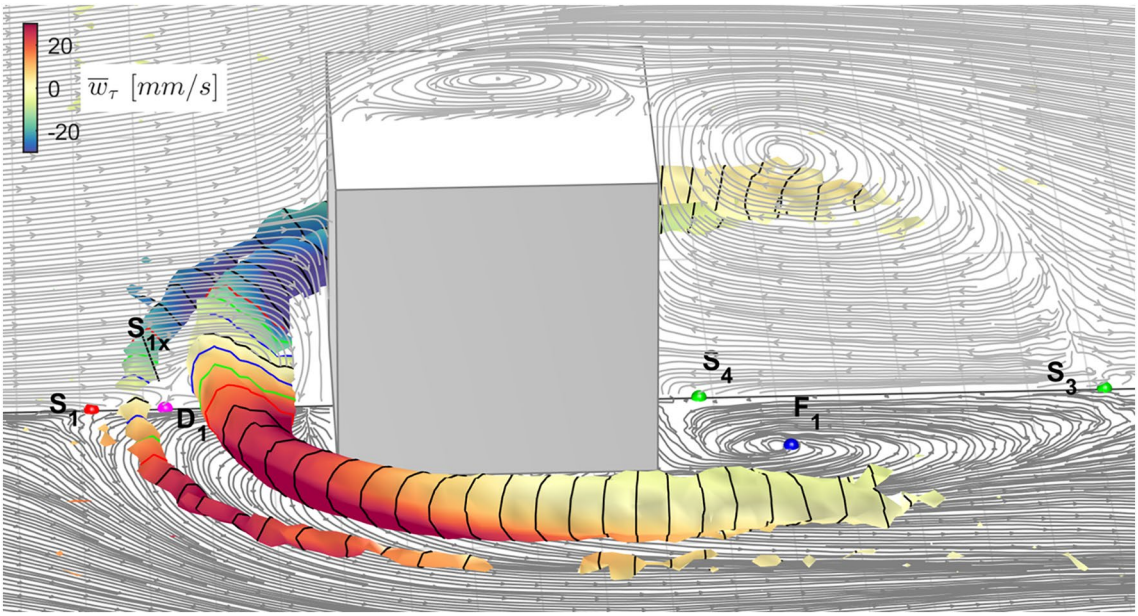

Fig. 15 Limiting streamlines topology of $\overline{\boldsymbol{U}}_V$ on horizontal plane $Y^+ = 4.6$ (horizontal) and streamlines topology of $\overline{\boldsymbol{U}}_V$ on vertical plane $Z^+ = 0$, together with the $\lambda_2 = -0.00075$ iso-surface capturing the horseshoe vortices system. Colored spheres report the position of the critical points S_1, S_4, D_1, and F_1 obtained from $\overline{\boldsymbol{U}}_{\tau_T}$ and reported in Fig. 16a

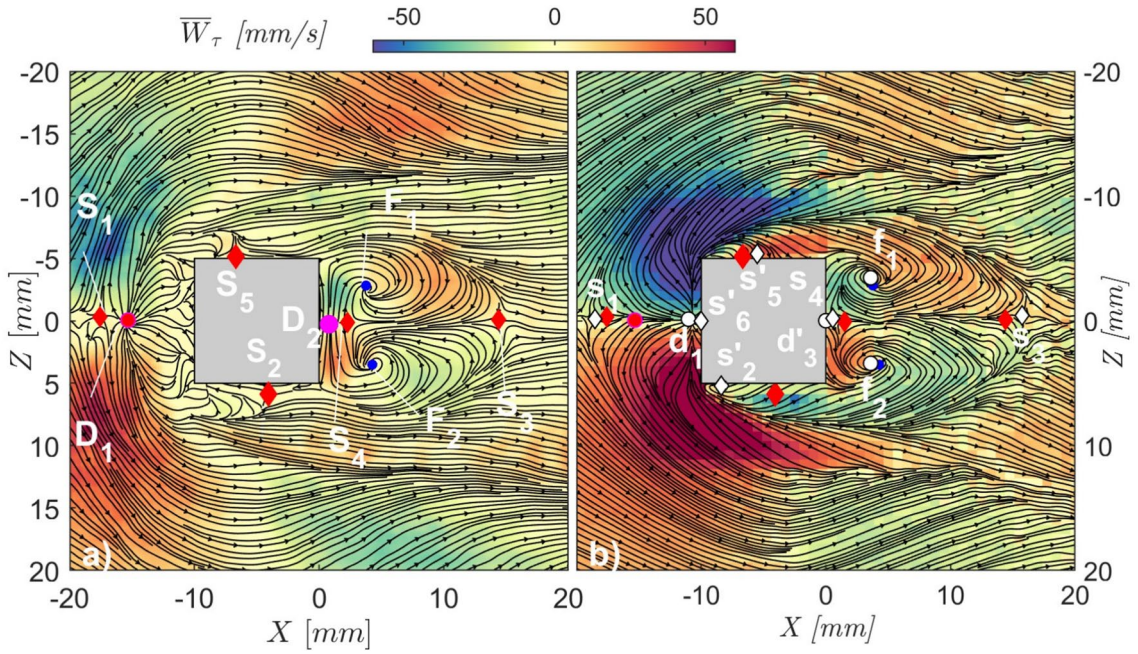

Fig. 16 Topology of $\overline{\boldsymbol{\tau}}$ around the cube overlapped to the spanwise friction velocity $\overline{W}_\tau$. Uppercase and lowercase letters mark critical points in $\overline{\boldsymbol{\tau}}_T$ (red, blue and crimson markers) and $\overline{\boldsymbol{\tau}}_V$ (white markers) respectively. The apex identifies the half-critical nodes of $\overline{\boldsymbol{\tau}}_V$ on the cube's border. **a** Topology of $\overline{\boldsymbol{\tau}}_T$ at $Y^+ = 0$. **b** Topology of $\overline{\boldsymbol{\tau}}_V$ at $Y^+ = 2.7$. Critical points of $\overline{\boldsymbol{\tau}}_T$ are reported both in **a** and **b** for easier comparison

Fig. 15 describing rotational regions and $\boldsymbol{U}_V$ topology from STB and Fig. 16 about the $\boldsymbol{\tau}$ topology from both STB and TSP. Critical points in the $\boldsymbol{\tau}_T$ abd $\boldsymbol{\tau}_V$ topologies are named in upper and lower case, respectively.

Front. The $\overline{\boldsymbol{U}}_{\tau_T}$ topology at the wall in Fig. 16a shows the signature, in the region immediately upstream of the cube, of a saddle-node S_1, where the incoming flow separates. The unstable manifolds emitted from S_1 symmetrically expand spanwise around the obstacle and then turn downstream, delimiting the outermost border of the influence region of the horseshoe vortex. The converging manifold from downstream connects S_1 to the diverging node D_1 along the center line. The flow reattaches at D_1 and, further downstream, undergoes another separation close to the obstacle.

The location of S_1 by TSP is found at $0.77H$ upstream of the cube side, a value comparable to $0.8H$ reported by Martinuzzi and Tropea (1993) at $Re_h = 40000$ (Fig. 14 within), and quite close to the s_1 saddle point outcoming from STB data, placed at 0.83H. The stagnation point D_1 is at $\approx$ 0.6H, and the further separation closer to the cube is at 0.2H.

The reattachment at the diverging node D_1 is an occurrence not reported by STB data or literature. This is a significant topological difference between the topologies of $\boldsymbol{u}_{\tau_V}$ and $\boldsymbol{u}_{\tau_T}$: while the $\boldsymbol{u}_{\tau_T}$ separation point S_1 is located $\approx$ 1 mm slightly downstream of the correspondent separation point s_1 of $\overline{\boldsymbol{\tau}}_V$, the reattachment node D_1 reported in $\boldsymbol{u}_{\tau_T}$ (Fig. 16a) cannot be identified in $\boldsymbol{u}_{\tau_V}$ vector field (Fig. 16b). Moreover, the first saddle point in Fig. 16b is located in correspondence to the diverging node D_1 (Fig. 16a). As a consequence, the flow region upstream of the separation close to the cube is oriented downward in $\boldsymbol{u}_{\tau_T}$, and upward in $\boldsymbol{u}_{\tau_V}$.

Based on the well-established coincidence between the topology of the wall shear stress $\boldsymbol{\tau}$ and the limiting streamlines ($\lim_{Y\to 0}$) of $\boldsymbol{U}$, Fig. 15 provides details about the horseshoe vortex and the topology of $\overline{\boldsymbol{U}}_V$ at two orthogonal planes, one horizontal at $Y^+ = 4.6$ (at the node closest to the wall) and one vertical at the symmetric location $Z^+ = 0$. The λ_2 criterion (Jeong and Hussain 1995) applied to the 3D STB data, binned on an isotropic grid, identifies two iso-surfaces at $\lambda_2 = -0.00075$ that capture the existence of two horseshoe-like vortices: a weaker, narrow one upstream, and a bigger, stronger one immediately downstream.

Remarkable peculiarities and differences between $\overline{\boldsymbol{\tau}}_V$ and $\overline{\boldsymbol{\tau}}_T$ topologies on the front side of the cube are:

- $\overline{\boldsymbol{U}}_V$ topology at $Y^+ = 4.6$ exhibits the saddle point s_1 just upstream of the weaker vortex. The location of s_1 corresponds quite well to that of S_1 in the $\overline{\boldsymbol{\tau}}_T$ vector field topology (red sphere at the plane crossing).
- In the $\overline{\boldsymbol{U}}_V$ topology, the saddle s_1 is the point where the incoming and the reverse flow converges. There, the separating flow ejected upward gives rise to the rotational structures developing upstream, identified in Fig. 15 by the λ_2 criterion.
- On the contrary, the $\overline{\boldsymbol{\tau}}_T$ topology embeds the weaker structure between the saddle S_1 and the diverging node D_1 (crimson sphere at the plane crossing) locations. This last node doesn't exist in either 2D (Fig. 5c) or 3D (Fig. 15) $\overline{\boldsymbol{\tau}}_V$ measurements (Fig. 16b). Numerical results don't report the diverging node D_1 as well.
- The $\overline{\boldsymbol{\tau}}_V$ streamlines below the horseshoe structures are oriented upstream, while the $\overline{\boldsymbol{\tau}}_T$ ones head downstream.

Summarizing, the topology of $\overline{\boldsymbol{\tau}}_T$ is in good agreement with that of $\overline{\boldsymbol{U}}_U$ up to the critical point S_1. Conversely, its downstream orientation is hard to justify from a fluid dynamic point of view when considering the large recirculating region of the horseshoe vortex and the results from 2D and 3D STB measurements (Schröder et al. 2020).

We can speculate this misalignment originates from the nature of the proposed measurement system, which relies on the existence of two main conditions:

- Fluid structures at the wall activated by the turbulent regime or, when in laminar condition, by some instability (e.g. the Goertler one among the others).
- A temperature gap between the body surface and the external flow, mild enough to keep the Richardson number below its critical value to avoid inducing spurious convective phenomena.

These two conditions guarantee the temperature fluctuations at the wall have a fine-scale pattern, because of the different heat exchange efficiencies associated with the local fluid structures. This fine-scale pattern identifies the different thermal blobs and provides the seeding of the TH algorithm.

The pierced cube proposed in the present setup is made of glass and is not in thermal connection with the heated wall below. The downstream flow impinges on the front surface at a distance of $\approx$ 7 mm from the wall (Fig. 5) and isn't exposed to any thermal characterization. The fluid moving along the down-oriented streamlines approaches the wall in a homogeneous thermal state, and the identity lack of thermal fluctuations jeopardizes their use in identifying the propagation of coherent structures. This miss of signal is at the origin of the misinterpretation by the TH algorithm of the flow behavior.

On the contrary, as shown in the following and Sect. 6.5, on the cube's rear side the flow impacts against the obstacle after sliding upstream on the heated surface, and the wall shear stress topology recorded by $\overline{\boldsymbol{\tau}}_T$ and $\overline{\boldsymbol{\tau}}_V$ is almost overlapped.

Side—The deceleration of the flow around the lateral edges of the cube induces the formation of a vertical vortex

which inverts its direction symmetrically on both sides of the obstacle. This behavior can be observed, by a different degree of symmetry, in the topology of the saddle points S_2, S_5 and s'_2, s'_5 respectively.

A different response in the two datasets can be observed downstream of the just-described saddle points where $\overline{\boldsymbol{\tau}}_T$ reports a collapse of the streamlines against the cube's lateral faces. We suppose this result is questionable and again, its origin can be ascribable to the flow sliding on the obstacle's side before impinging against the wall without a thermal characterization. Lagrangian info on such a flow circulation can be found in da Silva et al. (2024) and Fig. 14b within.

Rear—Around the corner, the flow decelerates under the influence of the adverse pressure gradient. There, it starts the onset of a reverse flow and the development of vertically oriented coherent structures induced by the cube corners' lateral edges. Both the topologies of $\overline{\boldsymbol{\tau}}_T$ and $\overline{\boldsymbol{\tau}}_V$ show the outer flow reattaching in the far wake, on the downstream centerline, at the saddle points S_3 and s_3 respectively. At that place, streamlines from the cube's sides converge as stable manifolds on the plane, while the unstable manifolds on the same plane diverge downstream and upstream. Downstream, the flow continues its pathway between the two branches of the horseshoe vortex. The flow along the upstream-headed manifold moves toward the obstacle and separates at the critical manifold $F_1 - S_4 - F_2\,(f_1 - s_4 - f_2)$. The separation point S_4 is located $0.1H$ downstream of the cube, close to s_4. The existence of s_4 (S_4) from the topology of $\overline{\boldsymbol{\tau}}$ is confirmed from both temperature and velocity data. The two large counter-rotating structures at both sides of the manifold $S_3 - S_4$ capture the arc-vortex signature at the wall, characterizing the rear side of the obstacle. The locations of spiral points in the pairs $F_1 - f_1$ and $F_2 - f_2$ from $\overline{\boldsymbol{\tau}}_T$ and $\overline{\boldsymbol{\tau}}_V$ are almost overlapped.

However, discrepancies arise between the saddle $S_4 - s_4$ and the back face of the cube. According to literature data see da Silva et al. (2024), among the others, the topology of $\overline{\boldsymbol{\tau}}_T$ reports the diverging node D_2 reconnecting the arch-like vortex flow to the wake. This critical point cannot be identified in the topology of $\overline{\boldsymbol{\tau}}_V$ as extracted from the 3D STB data binned on the non-isotropic grid. The failure in d_1 identification is most probably due to a resolution issue, being the reminiscence of a diverging node still visible in the isotropic one, because of its higher horizontal resolution.

Results are compatible with Martinuzzi and Tropea (1993), but the direct comparison is not available due to their measurement technique, because the oil film disappears within the two recirculating regions. Based on the Poincaré-Bendixson theory, we follow (Hunt et al. 1978; Foss et al. 2016) to check the topological integrity of the skin friction field outcomes through the topological rule (Hunt et al. 1978; Foss et al. 2016):

$$\left(\sum N + \frac{1}{2}\sum N'\right) - \left(\sum S + \frac{1}{2}\sum S'\right) = 1 - n \qquad (16)$$

In Eq. 16, N are nodes and focuses, while S are the saddle points. The apex identifies the half-critical nodes, and $n = 2$ is the coefficient for a doubly-connected domain. The vector field $\boldsymbol{\tau}_V$ successfully complies with Eq. 16 as $(3 + 0.5) - (3 + 1.5) = -1$. The noise measured upstream of the cube's front side jeopardizes the vector field's check of $\boldsymbol{\tau}_T$.

6.5 Magnitude comparison

This section reports an assessment attempt of the accuracy of the proposed method based on the comparison of the magnitude of the friction velocity components as obtained from temperature ($\overline{\boldsymbol{u}}_{\tau_T}$) and velocity ($\overline{\boldsymbol{u}}_{\tau_V}$) data. The matching between the topology backbones of $\overline{\boldsymbol{u}}_{\tau_T}$ and $\overline{\boldsymbol{U}}_{\tau_{V_{WN}}}$ described in the previous section simplifies the comparison of the outcome data magnitude. Streamwise $\overline{u}_\tau$ and spanwise $\overline{w}_\tau$ skin friction components are reported in Fig. 17, top row for $\overline{\boldsymbol{u}}_{\tau_V}$ and bottom row for $\overline{\boldsymbol{u}}_{\tau_T}$. The lack of particles and signal in the downstream region of $\overline{\boldsymbol{u}}_{\tau_V}$ jeopardizes the correct estimation of the local velocity. That region has been blanketed as a consequence.

The magnitude comparison of $\overline{\boldsymbol{u}}_{\tau_T}$ and $\overline{\boldsymbol{u}}_{\tau_V}$ components along streamwise and spanwise sections provide a meaningful sketch of the differences between the two datasets, see Figs. 18 and 19. Section locations are numbered from 1 to 8, and reported as dash-dotted lines, in Fig. 17.

Results about $\overline{\boldsymbol{u}}_{\tau_V}$ components report profiles picked at the first node of the non-isotropic grid, placed at $Y^+ = 2.7$ (red line).

Error bars of $\overline{\boldsymbol{u}}_{\tau_T}$ in Figs. 18 and 19 report the uncertainty of the ratio in Eq. 4, where the variances of numerator and denominator have been calculated based on the variances of the measured distributions ∂_1, ∂_2, and ∂_t. This info allows calculating the variance of the mean of their product (e.g. $\overline{\partial_1\partial_2}$) and of the linear combination of the product of their mean (e.g. $-\overline{(\partial_1)^2}\cdot\overline{\partial_1\partial_t} + \overline{\partial_1\partial_2}\cdot\overline{\partial_2\partial_t}$). The variance of the ratio Var provides the uncertainty of the mean by $\delta = \sqrt{Var}/\sqrt{N}$, where $N = 6339$ is the number of measured velocity fields.

At section 1 upstream of the cube, the $\overline{U}_{\tau_V}$ profile marks the existence of a reverse flow region on the centerline (Fig. 18a), whose existence is missed by $\overline{U}_{\tau_T}$. On the contrary, the comparison of the spanwise components $\overline{W}_{\tau_V}$ and $\overline{W}_{\tau_T}$ at the same section (Fig. 18b) reports an excellent agreement, with slight amplitude differences around

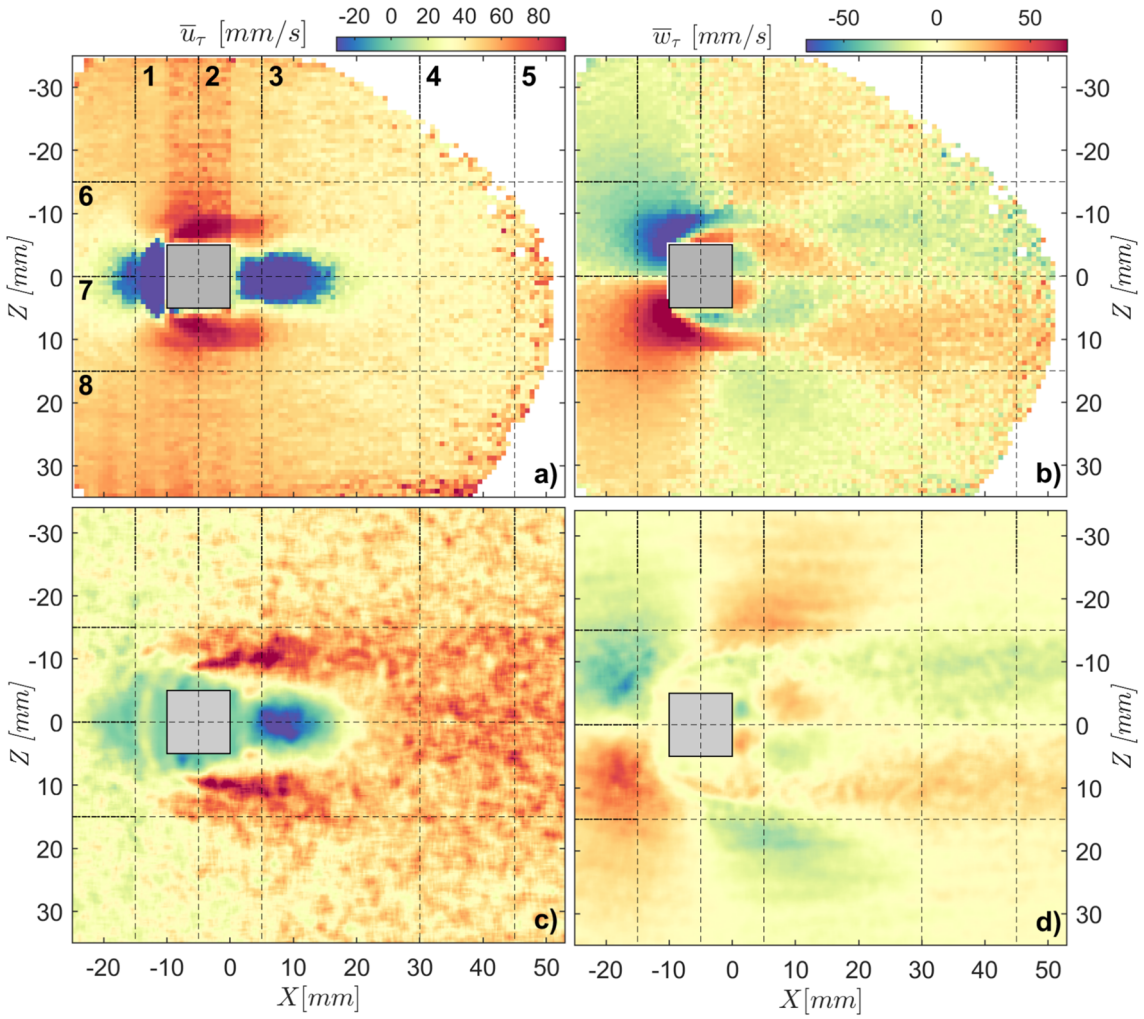

Fig. 17 Streamwise (**a** and **c**) and spanwise (**b** and **d**) friction velocity components of $\boldsymbol{u}_{\tau_V}$ (top, **a** and **b**) and $\boldsymbol{u}_{\tau_T}$ (bottom, **c** and **d**)

the positive and negative peaks. This result confirms the relevance of the thermal characterization of the streamwise flow. It also shows how the issue is minimized, in the same locations, if the spanwise flow displacement allows for its thermal characterization.

At section 2 across the cube, streamwise components overlap quite well (Fig. 18c), with slight differences in peak intensities close to the obstacle. The spanwise components show strong differences close to the cube, that strongly reduce at increasing distances (Fig. 18d), then converge toward zero. This confirms the topological results around the saddle points S_2 and S_5, where the spanwise component signature is strongly affected by the thermally homogeneous flow sliding on the lateral cube faces.

At section 3 in the cube wake, both $\overline{u}_\tau$ and $\overline{v}_\tau$ components show an excellent agreement (Figs. 18ef). Peaks' location and intensity are well captured, and profiles overlap farther from the middle line.

At section 4 in the near wake, the streamwise components still show a good agreement (Fig. 18g), while the profiles of the spanwise components perfectly overlap (Fig. 18h).

At section 5 in the far wake, $\overline{u}_\tau$ components show a similar order of magnitude (Fig. 18i). The profiles of the spanwise components convincingly overlap (Fig. 18l).

Section 6 and section 8 are located symmetrically on the obstacle's sides. They report a mirrored behavior of $\overline{u}_\tau$ and $\overline{\boldsymbol{u}}_{\tau_V}$. The $\overline{u}_\tau$ components have comparable values and evolve with a similar evolution along the path (Fig. 19ac), The $\overline{w}_\tau$ spanwise component evolutions are in excellent agreement, being the two quantities $\overline{u}_{\tau_V}$ and $\overline{u}_{\tau_T}$ separated by a phase delay when they are next to the cube (Fig. 19bd) .

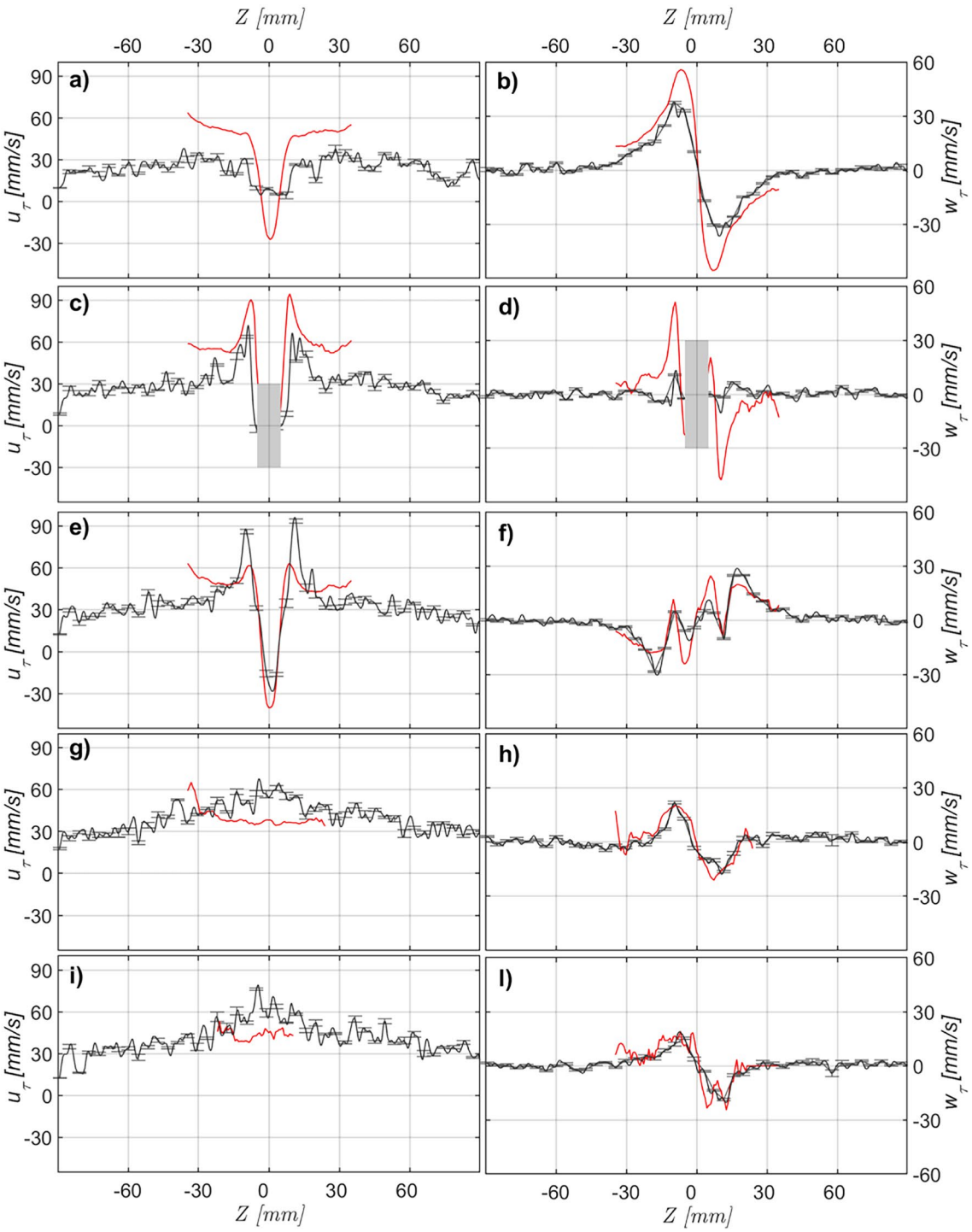

Fig. 18 Comparison of $\overline{\boldsymbol{u}}_{\tau_T}$ (gray lines) and $\overline{\boldsymbol{u}}_{\tau_V}$ (red line) components magnitude along the five spanwise sections reported as vertical dash-dotted lines in Fig. 17: $1 \rightarrow a-b$, $2 \rightarrow c-d$, $3 \rightarrow e-f$, $4 \rightarrow g-h$, $5 \rightarrow i-l$. $\overline{\boldsymbol{u}}_{\tau_V}$ data have been picked at the grid nodes closer to the wall of the non-isotropic grid, i.e. at $Y^+ = 2.7$. The error bars report the uncertainty of the mean in Eq. 4

At section 7 along the middle line upstream of the cube, the profiles of $\overline{\boldsymbol{u}}_{\tau_V}$ and $\overline{\boldsymbol{u}}_{\tau_T}$ show the differences already discussed downstream the saddle-point S_1. Upstream of S_1 and within the obstacle wake along the middle line the evolution of the streamwise components coincides, and their

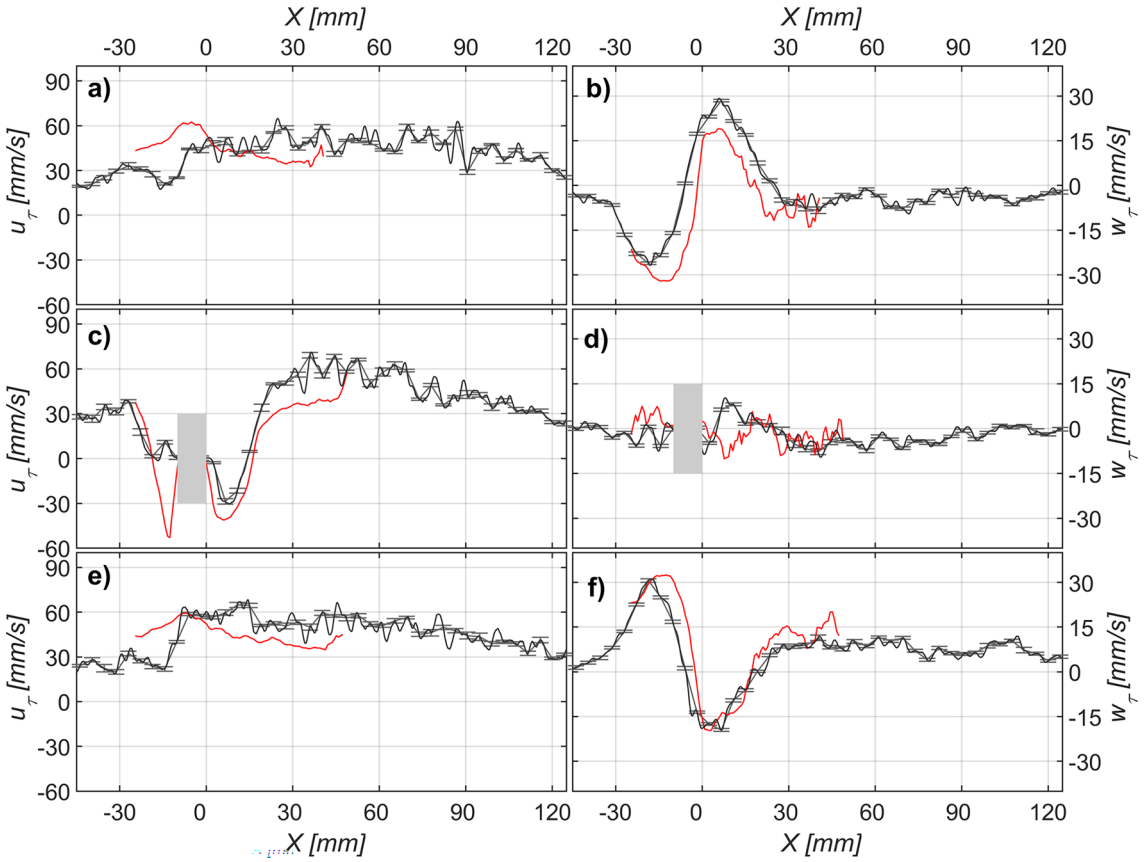

Fig. 19 Comparison of the $\overline{\boldsymbol{u}}_{\tau_T}$ (gray lines) and $\overline{\boldsymbol{u}}_{\tau_V}$ (red lines) components magnitude along the three streamwise sections reported as horizontal dash-dotted lines in Fig. 17: $6 \rightarrow a-b$, $7 \rightarrow c-d$, $8 \rightarrow e-f$. $\overline{\boldsymbol{u}}_{\tau_V}$ data have been picked at the node closer to the wall of the non-isotropic grid, i.e. at $Y^+ = 2.7$. The error bars report the uncertainty of the mean in Eq. 4

overlap is excellent. The magnitude of $\overline{v}_{\tau_T}\,\overline{v}_{\tau_V}$ is almost negligible everywhere, as expected by the spanwise component along the middle line in a streamline-aligned reference system (Fig. 19ef).

7 Conclusions

We report the latest developments on time-averaged skin friction estimation by a method based on time-resolved temperature maps collected by TSP and on a relaxed version of the Taylor Hypothesis. The report introduces the theoretical hypothesis in the background of the algorithm and then proposes its application to the flow around a wall-mounted cube. The assessment of the results compares the wall shear stress topology and its intensity against the outcomes of 2D and 3D STB campaigns, performed on the same facility at the same flow conditions.

The relaxation of the *frozen turbulence* hypothesis leads to a minimization problem involving the Lagrangian derivative of the investigated fluid dynamic quantity, which contains a nonlinearity introduced by the double product between $U_{q_1}\partial_1$ and $U_{q_2}\partial_2$ (Eq. 4). The resulting two-unknowns, two-equations system brings a relaxed expression of the Taylor Hypothesis for the U_q velocity components of the passive tracer q which is still valid at the wall, where the full form of the Taylor Hypothesis doesn't hold. The system inherits the nonlinearity as a mutual dependence between the U_q components. This dependence is negligible in straight flows with minor spanwise velocity. On the contrary, in flows where the cross-correlation $\partial_1\partial_2 \neq 0$ doesn't vanish, it can contribute to a considerable part, as shown in the wall-pierced cube application.

The comparative analysis of the skin-friction-related quantities obtained from temperature ($\overline{\boldsymbol{\tau}}_T$) and velocity ($\overline{\boldsymbol{\tau}}_V$) data relies on a topological comparison to get a sketch of the equivalence's degree between the essential flow backbones. This preparatory analysis provides the topological framework for the vector fields' magnitude comparison.

Despite a general topological equivalence, the region upstream of the cube between the saddle point $S_1 - s_1$

and the front face of the obstacle reports opposite outcomes from $\overline{\boldsymbol{u}}_{\tau_T}$ and $\overline{\boldsymbol{u}}_{\tau_V}$. 2D and 3D STB results, as well as literature data, show the existence of two co-rotating, horseshoe-shaped flow structures, a narrow upstream and a wider downstream, that force the flow at the wall to head upstream.

We conjectured the origin of the problem lies in the lack of thermal characterization of the incoming flow. This thermally homogeneous flow is pushed downward after the stagnation point on the front side of the cube. The protrusion is thermally disconnected from the heated wall because it is made of glass, and its surface is not heated in any other way. This way, the flow impacting against the wall lacks thermal characterization and provides no signal to the temperature field. A similar flow condition can be observed close to the lateral sides of the cube.

Downstream of the obstacle, the topological agreement between the skin friction from temperature and velocity data is excellent: both the reattachment in the wake ($S_3 \equiv s_3$) and the foci at the roots of the arch-shaped vortex ($F_1 \equiv f_1$ and $F_2 \equiv f_2$) almost overlap. Diverging node D_2 in the $\overline{\boldsymbol{u}}_{\tau_T}$ topology is missed in the $\overline{\boldsymbol{u}}_{\tau_V}$ one, most probably because of a lack in the horizontal resolution of the non-isotropic grid.

About the alteration of the heat flux across the TSP layer induced by the presence of the adiabatic cube and its effects on $\overline{\boldsymbol{u}}_{\tau_T}$, it seems reasonable to assume it is isotropic in all directions. Given that its effect is negligible downstream of the cube, we argue that its influence is of minor importance on the skin friction estimation by TSP.

The topological framework depicted so far allows for an easy interpretation of the similarities and discrepancies between the profiles of skin friction extracted along different sections. There is a general agreement between the $\overline{\boldsymbol{u}}_{\tau_T}$ and $\overline{\boldsymbol{u}}_{\tau_V}$ outcomes, that supports the feasibility of the TSP in estimating the time-averaged skin friction field.

The convective velocity dependence on the wavenumber is managed following the work of Kim and Hussain (1993) and Del Álamo and Jiménez (2009), as described in Sect. 3.1. A more detailed analysis of the temperature fluctuations celerity in the frequency-wavenumber spectrum is postponed to future work.

In conclusion, it is to remark on the role of *Rosetta stone* played by the 2D STB in connecting results obtained by TSP to the outcomes from the velocity field. The time-resolved snapshots of the 2D-2C velocity data allow us to compare two friction velocity profiles obtained via two different methods applied to the same dataset. The comparison between the wall-normal derivative and the TH algorithm furnishes a quantitative estimation of c_U, representing the proportionality factor between the celerity of the velocity fluctuations U_U and the friction velocity U_τ. This coefficient, modulated by the Prantl-related c_T coefficient (Hetsroni et al. 2004), has been used to estimate $\overline{\boldsymbol{u}}_{\tau_T}$. The degree of overlap shown by the two friction velocity estimations just before the front side of the cube, obtained using a constant proportionality factor, is also a clue of both the correctness of the coefficient c_T proposed by Hetsroni et al. (2004) to take into account the $Pr \neq 1$ fluid condition and the weak dependence of c_U on the pressure gradient.

As a final comment, it should be observed that the ability to acquire high spatial resolution data of large regions of the investigated surface, with sampling frequencies recently elevated to 40 kHz and more (see e.g. Bitter et al. 2022 on ultra-Fast TSP for air flows) promotes the leading role that TSP can play in supporting the fine-tuning of the loci around which it is worth focusing the search for flow details.

This is one of the first attempts to compare the wall shear stress between data sets obtained from velocity data and temperature fluctuations in a complex flow condition. The challenging nature of the flow makes this effort not straightforward and representative. At the same time, the positive lesson learned by approaching the issues in comparing TSP and STB outcomes unveils the potential of combining surface and flow information in near-wall fluid dynamic studies.

Acknowledgements The authors would like to thank Mrs. Marie-Claire Merienne (ONERA), Mr. Jacquest Pruvost (ONERA) and Dr. Reinhard Geisler (DLR) for their assistance during the setup of the experiment and measurements. DLR internal project funding devoted to DLR-ONERA Common Research Project CUBE and CUBE2.

Funding Open access funding provided by Consiglio Nazionale Delle Ricerche (CNR) within the CRUI-CARE Agreement.

References

Asai K, Kanda H, Kunimasu T, Liu T, Sullivan JP (1996) Detection of boundary-layer transition in a cryogenic wind tunnel by using luminescent paint. In: AIAA, advanced measurement and ground testing technology conference, 19th, New Orleans, LA, June 17–20, 1996. https://doi.org/10.2514/6.1996-2185 . AIAA 1996-2185

Astarita T, Carlomagno GM (2012) Infrared Thermography for thermo-fluid-dynamics. Experimental fluid mechanics. Springer, Berlin, Heidelberg. https://doi.org/10.1007/978-3-642-29508-9

Baker CJ (1980) The turbulent horseshoe vortex. J Wind Eng Ind Aerodyn 6(1–2):9–23. https://doi.org/10.1016/0167-6105(80)90018-5

Bitter M, Hilfer M, Schubert T, Klein C, Niehuis R (2022) An ultra-fast TSP on a CNT heating layer for unsteady temperature and heat flux measurements in subsonic flows. Sensors. https://doi.org/10.3390/s22020657

Capone A, Klein C, Di Felice F, Beifuss U, Miozzi M (2015) Fast-response underwater TSP investigation of subcritical instabilities of a cylinder in crossflow. Exp Fluids 56(10):1–14. https://doi.org/10.1007/s00348-015-2065-9

Cattafesta LN, Liu T, Sullivan JP (1998) Uncertainty estimates for temperature-sensitive paint measurements with charge-coupled device cameras. AIAA J 36(11):2102–2108. https://doi.org/10.2514/2.313

da Silva BL, Sumner D (2024) Revisiting the surface-mounted cube: An updated perspective of the near wake and near-wall flow field. Int J Heat Fluid Flow 106:109288. https://doi.org/10.1016/j.ijheatfluidflow.2024.109288

Del Álamo JC, Jiménez J (2009) Estimation of turbulent convection velocities and corrections to Taylor's approximation. J Fluid Mech 640:5–26. https://doi.org/10.1017/S0022112009991029

Depardon S, Lasserre JJ, Boueilh JC, Brizzi LE, Borée J (2005) Skin friction pattern analysis using near-wall PIV. Exp Fluids 39(5):805–818. https://doi.org/10.1007/s00348-005-0014-8

Diaz-Daniel C, Laizet S, Vassilicos J-C (2017) Direct numerical simulations of a wall-attached cube immersed in laminar and turbulent boundary layers. Int J Heat Fluid Flow 68:269–280. https://doi.org/10.1016/j.ijheatfluidflow.2017.09.015

Dróżdż A, Niegodajew P, Romańczyk M, Elsner W (2023) Convection velocity in turbulent boundary layers under adverse pressure gradient. Exp Therm Fluid Sci. https://doi.org/10.1016/j.expthermflusci.2023.110900

Eckelmann H (1974) The structure of the viscous sublayer and the adjacent wall region in a turbulent channel flow. J Fluid Mech 65(3):439–459. https://doi.org/10.1017/S0022112074001479

Egami Y, Klein C, Henne U, Bruse M, Ondrus V, Beifuss U (2009) Development of a highly sensitive temperature-sensitive paint for measurements under ambient (0 – 60° C) conditions. In: 47th AIAA aerospace sciences meeting including the new horizons forum and aerospace exposition. https://doi.org/10.2514/6.2009-1075

Fey U, Egami Y (2007) Transition-detection by temperature-sensitive paint. In: Tropea C, Yarin AL, Foss JF (eds) Springer handbook of experimental fluid mechanics. Springer, Heidelberg, Berlin. https://doi.org/10.1007/978-3-540-30299-5_7

Foss JF, Hedden M, Barros JM, Christensen KT (2016) A topological evaluation procedure to assess the integrity of a PIV vector field. Meas Sci Technol. https://doi.org/10.1088/0957-0233/27/9/094007

Gao J, Agarwal K, Katz J (2021) Experimental investigation of the three-dimensional flow structure around a pair of cubes immersed in the inner part of a turbulent channel flow. J Fluid Mech. https://doi.org/10.1017/jfm.2021.184

Gartenberg E, Johnson WG, Johnson CB, Carraway DL, Wright RE (1990) Transition detection studies in the cryogenic environment. In: Flight simulation technologies conference and exhibit. https://doi.org/10.2514/6.1990-3024. AIAA 90-3024

Geng C, He G, Wang Y, Xu C, Lozano-Durán A, Wallace JM (2015) Taylor's hypothesis in turbulent channel flow considered using a transport equation analysis. Phys Fluids 27(2):025111. https://doi.org/10.1063/1.4908070

Hetsroni G, Tiselj I, Bergant R, Mosyak A, Pogrebnyak E (2004) Convection velocity of temperature fluctuations in a turbulent flume. J Heat Transf 126(5):843–848. https://doi.org/10.1115/1.1797032

Hunt JCR, Abell CJ, Peterka JA, Woo H (1978) Kinematical studies of the flows around free or surface-mounted obstacles; applying topology to flow visualization. J Fluid Mech 86(1):179–200. https://doi.org/10.1017/S0022112078001068

Jahn T, Schanz D, Schroöder A (2021) Advanced iterative particle reconstruction for Lagrangian particle tracking. Exp Fluids 62:179. https://doi.org/10.1007/s00348-021-03276-7

Jeong J, Hussain F (1995) On the identification of a vortex. J Fluid Mech 285:69–94. https://doi.org/10.1017/S0022112095000462

Kim J, Hussain F (1993) Propagation velocity of perturbations in turbulent channel flow. Phys Fluids A 5(3):695–706. https://doi.org/10.1063/1.858653

Klein C, Henne U, Sachs W, Beifuß U, Ondrus V, Bruse M, Lesjak R, Löhr M (2014) Application of carbon nanotubes (CNT) and temperature-sensitive paint (TSP) for the detection of boundary layer transition. In: 52nd Aerospace sciences meeting, 13–17 January 2014, National Harbor. https://doi.org/10.2514/6.2014-1482. AIAA 2014-1482

Klein C, Yorita D, Henne U, Ondrus V, Hensch A-K, Longo Gimbel A, Deetzen S (2020) Application of temperature sensitive paint to investigate laminar-to-turbulent transition on nacelles. In: AIAA Scitech 2020 forum, 6–10 January 2020, Orlando. https://doi.org/10.2514/6.2020-1608 . AIAA 2020-1608

Klein C, Lemarechal J, Henne U, Koch S, Ondrus V, Hensch A-K, Schaber S (2023) Temperature-sensitive paint measurements in combination with carbon-fiber-reinforced plastic models in cryogenic conditions. In: AIAA SCITECH 2023 forum, 23–27 January 2023, National Harbor, MD & Online (2023). https://doi.org/10.2514/6.2023-1460. AIAA 2023-1460

Koenderink JJ (1984) The structure of images. Biol Cybern 50(5):363–370. https://doi.org/10.1007/BF00336961

Lemarechal J, Klein C, Henne U, Puckert DK, Rist U (2019) Detection of lambda- and omega-vortices with the temperature-sensitive paint method in the late stage of controlled laminar-turbulent transition. Exp Fluids 60(91):1–14. https://doi.org/10.1007/s00348-019-2734-1

Lemarechal J, Klein C, Puckert DK, Rist U (2021) Application of the temperature-sensitive paint method for quantitative measurements in water. Meas Sci Technol. https://doi.org/10.1088/1361-6501/ac0333

Liu T, Campbell BT, Sullivan JP, Lafferty J, Yanta W (1995) Heat transfer measurement on a Waverider at Mach 10 using fluorescent paint. J Thermophys Heat Transf 4(9):605–611. https://doi.org/10.2514/3.714

Liu T, Campbell B, Sullivan J (1995) Accuracy of temperature-sensitive fluorescent paint for heat transfer measurements. In: 30th AIAA thermophysics conference, 19–22 June 1995, SanDiego, CA, USA. https://doi.org/10.2514/6.1995-2042

Liu T, Sullivan JP, Asai K, Klein C, Egami Y (2021) Pressure and temperature sensitive paints. Experimental fluid mechanics. Springer, Berlin, Heidelberg. https://doi.org/10.1007/978-3-030-68056-5

Liu T, Chen T, Miozzi M (2024) Correlation between skin friction and enstrophy convection velocity in near-wall turbulence. Eur J Mech B Fluids 104:224–230. https://doi.org/10.1016/j.euromechflu.2023.12.009

Mandracchia B, Hua X, Guo C, Son J, Urner T, Jia S (2020) Fast and accurate sCMOS noise correction for fluorescence microscopy. Nat Commun 11:1. https://doi.org/10.1038/s41467-019-13841-8

Martinuzzi R, Tropea C (1993) The flow around surface-mounted, prismatic obstacles placed in a fully developed channel flow: (data bank contribution). J Fluids Eng Trans ASME 115(1):85–92. https://doi.org/10.1115/1.2910118

Miozzi M (2005) Accuracy of C1 natural neighbors interpolation of feature tracking data and vorticity measurements. In:

6th International symposium on particle image velocimetry, CALTECH, Pasadena. https://hdl.handle.net/20.500.14243/465861

Miozzi M, Capone A, Klein C, Di Felice F (2015) Integrating high-frequency, time resolved TSP surface maps and wake flow Lagrangian description to investigate sub-critical regime in a crossflow cylinder. In: 11th International symphosium on particle image velocimetry-PIV2015 Santa Barbara, California, September 14–16, 2015, p. 26

Miozzi M, Capone A, Costantini M, Fratto L, Klein C, Di Felice F (2019) Skin friction and coherent structures within a laminar separation bubble. Exp Fluids 60:13. https://doi.org/10.1007/s00348-018-2651-8

Miozzi M, Di Felice F, Klein C, Costantini M (2020) Taylor hypothesis applied to direct measurement of skin friction using data from temperature sensitive paint. Exp Therm Fluid Sci 110:109913. https://doi.org/10.1016/j.expthermflusci.2019.109913

Nakakita K, Osafune T, Asai K (2003) Global heat transfer measurement in a hypersonic shock tunnel using temperature sensitive paint. In: 41'st AIAA Aerospace Sciences Meeting, 6–9. January, 2003, Reno, NV, USA. https://doi.org/10.2514/6.2003-743 . AIAA 2003-0743

Nakamura H (2009) Frequency response and spatial resolution of a thin foil for heat transfer measurements using infrared thermography. Int J Heat Mass Transf 52(21):5040–5045. https://doi.org/10.1016/j.ijheatmasstransfer.2009.04.019

Nekkanti A, Schmidt OT (2021) Frequency-time analysis, low-rank reconstruction and denoising of turbulent flows using spod. J Fluid Mech 926:26. https://doi.org/10.1017/jfm.2021.681

Ondrus V, Meier R, Klein C, Henne U, Schäferling M, Beifuss U (2015) Europium 1,3-di(thienyl)propane-1,3-diones with outstanding properties for temperature sensing. Sens Actuators A Phys 233:434–441. https://doi.org/10.1016/j.sna.2015.07.023

Örlü R, Vinuesa R (2020) Instantaneous wall-shear-stress measurements: advances and application to near-wall extreme events. Meas Sci Technol. https://doi.org/10.1088/1361-6501/aba06f

Ozawa H, Laurence S, Martinez Schramm J, Wagner A, Hannemann K (2014) Fast-response temperature-sensitive-paint measurements on a hypersonic transition cone. Exp Fluids 56:1853. https://doi.org/10.1007/s00348-014-1853-y

Risius S, Beck WH, Klein C, Henne U, Wagner A (2017) Determination of heat transfer into a wedge model in a hypersonic flow using temperature-sensitive paint. Exp Fluids 58(9):117. https://doi.org/10.1007/s00348-017-2393-z

Schanz D, Gesemann S, Schröder A, Wieneke B, Novara M (2013) Non-uniform optical transfer functions in particle imaging: calibration and application to tomographic reconstruction. Meas Sci Technol 24:024009. https://doi.org/10.1088/0957-0233/24/2/024009

Schanz D, Gesemann S, Schröder A (2016) Shake-the-box: Lagrangian particle tracking at high particle image densities. Exp Fluids 57:70. https://doi.org/10.1007/s00348-016-2157-1

Schlichting H, Gersten K (2017) Boundary-layer theory, 9th edn. Springer, Berlin, Heidelberg. https://doi.org/10.1007/978-3-662-52919-5

Schröder A, Schanz D (2023) 3D Lagrangian particle tracking in fluid mechanics. Annu Rev Fluid Mech 55(1):511–540. https://doi.org/10.1146/annurev-fluid-031822-041721

Schröder A, Schanz D, Novara M, Philipp F, Geisler R, Knopp T, Schroll M, Willert C (2018) Investigation of a high Reynolds number turbulent boundary layer flow with adverse pressure gradients using PIV and 2d-and 3d-Shake-The-Box. In: 19th International symposium on the application of laser and imaging techniques to fluid mechanics (2018). https://elib.dlr.de/121221/

Schröder A, Willert C, Schanz D, Geisler R, Jahn T, Gallas Q, Leclaire B (2020) The flow around a surface mounted cube: a characterization by time-resolved PIV, 3D Shake-The-Box and LBM simulation. Exp Fluids 61(9):3456. https://doi.org/10.1007/s00348-020-03014-5

Sibson R (1981) A brief description of natural neighbour interpolation. In: Barnett V (ed) Interpreting multivariate data. Wiley, Chichester, pp 21–36

Silva BL, Sumner D, Bergstrom DJ (2021) Mean and dynamic aspects of the wakes of a surface-mounted cube and block. J Fluids Eng 144(1):011302. https://doi.org/10.1115/1.4051428

Taylor GI (1938) The spectrum of turbulence. Proc Roy Soc Lond Ser A Math Phys Sci 164(919):476–490. https://doi.org/10.1098/rspa.1938.0032

Thévenaz P, Blu T, Unser M (2000) Interpolation revisited. IEEE Trans Med Imaging 19(7):739–758. https://doi.org/10.1109/42.875199

Tian Q, Simpson RL, Tang G (2004) Flow visualization on the linear compressor cascade endwall using oil flows and laser doppler anemometry. Meas Sci Technol 15(9):1910–1916. https://doi.org/10.1088/0957-0233/15/9/031

Tropea C, Yarin AL, Foss JF (2007) Springer Handbook of Experimental Fluid Mechanics. Springer, Berlin, Heidelberg. https://doi.org/10.1007/978-3-540-30299-5

Wieneke B (2008) Volume self-calibration for 3d particle image velocimetry. Exp Fluids 45:549–556. https://doi.org/10.1007/s00348-008-0521-5

Wieneke B (2012) Iterative reconstruction of volumetric particle distribution. Meas Sci Tech 24:024008. https://doi.org/10.1088/0957-0233/24/2/024008

Yakhot A, Liu H, Nikitin N (2006) Turbulent flow around a wall-mounted cube: a direct numerical simulation. Int J Heat Fluid Flow 27(6):994–1009. https://doi.org/10.1016/j.ijheatfluidflow.2006.02.026